The Astrophysical Journal, 911:70 (24pp), 2021 April 10 https://doi.org/10.3847/1538-4357/abe70c

Near-infrared Coronal Line Observations of Dwarf Galaxies Hosting AGN-driven Outflows

Thomas Bohn[1], Gabriela Canalizo[1], Sylvain Veilleux[2,3], and Weizhe Liu[2]
[1] University of California, Riverside, Department of Physics & Astronomy 900 University Avenue, Riverside, CA 92521, USA; tbohn002@ucr.edu
[2] Department of Astronomy, University of Maryland, College Park, MD 20742, USA
[3] Joint Space-Science Institute, University of Maryland, College Park, MD 20742, USA
Received 2020 December 28; revised 2021 February 8; accepted 2021 February 15; published 2021 April 16

Abstract

We have obtained Keck near-infrared spectroscopy of a sample of nine $M_\star < 10^{10}\ M_\odot$ dwarf galaxies to confirm active galactic nuclei (AGNs) activity and the presence of galaxy-wide, AGN-driven outflows through coronal line (CL) emission. We find strong CL detections in 5/9 galaxies (55%) with line ratios incompatible with shocks, confirming the presence of AGNs in these galaxies. Similar CL detection rates are found in larger samples of more massive galaxies hosting type 1 and 2 AGNs. We investigate the connection between the CLs and galaxy-wide outflows by analyzing the kinematics of the CL region as well as the scaling of gas velocity with ionization potential of different CLs. In addition, using complementary Keck Cosmic Web Imager observations of these objects, we find that the outflow velocities measured in [Si VI] are generally faster than those seen in [O III]. The galaxies with the fastest outflows seen in [O III] also have the highest [Si VI] luminosity. The lack of *J*-band CN absorption features, which are often associated with younger stellar populations, provides further evidence that these outflows are driven by AGNs in low-mass galaxies.

Unified Astronomy Thesaurus concepts: Active galactic nuclei (16); AGN host galaxies (2017); Dwarf galaxies (416); Seyfert galaxies (1447); Near infrared astronomy (1093); Active galaxies (17); Galaxy evolution (594)

1. Introduction

It is now well accepted that supermassive black holes (BHs) lie at the center of most massive galaxies. Strong correlations have supported the idea that they evolve with their host galaxies and feedback from the active galactic nuclei (AGNs) has been shown to regulate star formation (for a review, see Kormendy & Ho 2013). Powerful, AGN-driven outflows are believed to suppress star formation (Rupke et al. 2017; U et al. 2019) in high-mass galaxies, leading their hosts to the well-defined red sequence.

The general consensus regarding feedback in dwarf galaxies ($M_\star < 10^{10}\ M_\odot$) is that stellar processes, such as starbursts and supernovae (SNe), provide the main source of quenching (e.g., Veilleux et al. 2005, 2020; Heckman & Thompson 2017). However, the growing rate of AGN detections in dwarf galaxies (Reines et al. 2013; Moran et al. 2014; Sartori et al. 2015) necessitates a closer look at AGN feedback in the low-mass regime. Evidence of AGN-driven feedback in dwarf galaxies is already starting to emerge. Penny et al. (2018) presented a sample of dwarf galaxies with AGN line ratios and kinematically disturbed gas at their centers possibly due to AGN feedback. In addition, Bradford et al. (2018) found a sample of isolated (>1 Mpc), gas-depleted dwarfs with optical line ratios indicative of AGN activity, which suggests that AGNs may play a role in clearing gas from dwarf galaxies.

The shallower gravitational potential wells of dwarf galaxies allow feedback mechanisms to have a more profound effect on the global interstellar medium. Although this means dwarf galaxies are more susceptible to external environmental effects, strong outflows may be capable of driving gas beyond the dark matter halo. To investigate this possibility, Manzano-King et al. (2019, hereafter MK19) observed a sample of 29 isolated dwarf galaxies with optical and IR signatures suggestive of AGN activity. Nine of these show fast outflows with a median speed of $\sim$645 km s^{-1} higher than the median host escape velocities of $\sim$300 km s^{-1}. If the outflows are of AGN origin, this would suggest that AGN feedback could eject material beyond the dark matter halo and have a substantial impact on the star formation rate. Furthermore, follow-up integral field spectroscopy done by Liu et al. (2020, hereafter L20) of this sample showed spatially extended outflows up to 3 kpc in a number of these targets. In addition, they detected outflow velocities greater than 500 km s^{-1} in six of these galaxies. Indeed, a small but non-negligible fraction (up to 6%) of the ionized outflowing gas has the necessary speeds to escape their galaxy.

However, line ratios from star-forming processes can sometimes mimic those of AGNs, and some contamination exists between the AGNs and star-forming regions of the Baldwin, Phillips & Terlevich (hereafter BPT; Baldwin et al. 1981) diagram (e.g., Allen et al. 2008; Rich et al. 2011). Moreover, L20 found core-collapse SNe to be energetic enough to drive the mass outflow rates (3×10^{-3}–$0.3\ M_\odot\ \mathrm{yr}^{-1}$) seen in their sample, and thus the contribution of stellar processes in driving the outflows cannot be formally ruled out.

To further characterize the kinematics of outflows, coronal lines (CLs) have been used as an additional tracer of outflows. CLs are forbidden transitions from highly ionized (>100 eV) species with widths suggesting the CL region lies between the broad and narrow-line regions (De Robertis & Osterbrock 1984, 1986; Penston et al. 1984; Erkens et al. 1997; Rodríguez-Ardila et al. 2002, 2006). Due to the high energies needed for their ionization, CLs are excellent indicators of AGN activity. They are often observed blueshifted relative to the systemic velocity of the host galaxy and thus are believed to be linked with outflows. Müller-Sánchez et al. (2011) have measured outflow speeds upwards of 1500 km s^{-1} through CL emission, and the velocity fields suggest the outflows are of biconical shape with collimation likely due to the torus (see Standard Model, Antonucci 1993).

Table 1
Observation Log

Galaxy	Date (YYYY mm dd)	Redshift	Exp. Time[a]	Slit PA (degrees)	Ext. Ap. (arcsec)	S/N[b]	Airmass	Telluric
SDSS J010005.93-011058.89[c]	2017 10 28	0.05151	8 × 240 s	51	1.89	25	1.12	HD18571
SDSS J081145.29+232825.72	2019 01 24	0.01573	12 × 240 s	45	1.63	13	1.58	BD-001836
SDSS J084025.54+181858.99	2019 01 24	0.01498	8 × 240 s	101	1.63	17	1.34	HD74721
SDSS J084234.50+031930.68[d]	2019 01 24	0.02882	8 × 240 s	277	1.63	18	1.28	HD74721
SDSS J090613.76+561015.22[d]	2019 01 24	0.04664	12 × 240 s	239	1.51	20	1.31	HD92573
SDDS J095418.15+471725.11[d]	2019 01 24	0.03266	10 × 240 s	144	1.63	18	1.18	HD92573
SDSS J100551.18+125740.65[d]	2018 10 24	0.00949	6 × 240 s	65	1.90	23	1.60	HD77332
SDSS J100935.66+265648.99[d]	2019 01 24	0.01436	8 × 240 s	226	1.63	18	1.03	HD86986
SDSS J144252.78+205451.67	2019 01 24	0.04262	9 × 240 s	101	1.52	14	1.24	HD124773

Notes.
[a] Exposures were typically done in ABBA nodding.
[b] Average continuum signal-to-noise ratio (S/N) across all orders.
[c] SDSS J0100-0110 was observed with NIRSPEC. All other targets were observed with NIRES.
[d] Indicates galaxies with CL detections. See Section 3.3.

In this article, we present follow-up near-infrared (NIR) spectroscopy of the nine dwarf galaxies from MK19 and L20 that show optical AGN line ratios and fast outflows. Through NIR diagnostics, we aim to confirm the presence of AGN activity and characterize the outflows through NIR emission lines. Details of the sample selection, observations, and data reduction are summarized in Section 2. Analysis of the data, including spectra fitting and AGN diagnostics, are covered in Section 3. In Section 4, we discuss the NIR emission lines and outflow characteristics. Throughout this article, we adopt a standard Lambda cold dark matter osmology with $H_0 = 70\,\mathrm{km\ s^{-1}\ Mpc^{-1}}$, $\Omega_M = 0.3$, and $\Omega_\Lambda = 0.7$.

2. Data and Observations

2.1. Sample Selection

Our sample of nine dwarf galaxies is from the AGN sample of MK19. Briefly, Reines et al. (2013), Moran et al. (2014), and Sartori et al. (2015) have identified hundreds of dwarf galaxies with optical and IR signatures indicative of AGN activity. MK19 created a subsample of candidate AGNs whose optical line ratios place them above the star-forming region of the BPT and Veilleux & Osterbrock (1987, hereafter VO87) line ratio diagrams or that have He II λ4686 emission (see Shirazi & Brinchmann 2012). They obtained Keck Low Resolution Imaging Spectrometer (LRIS; e.g., Oke et al. 1995; Rockosi et al. 2010) spectroscopy of 29 of these galaxies, nine of which showed blue asymmetries in their [O III] λ5007 profile. This blue wing is often regarded as an indicator of outflowing gas, where the asymmetry arises due to the redshifted gas being blocked from our line of sight. These nine dwarf galaxies with spatially extended outflows form our sample for this article. Their stellar masses range from $8.77 < \log(M_*/M_\odot) < 9.97$ (median of 9.34), and all have a redshift of $z < 0.05$.

2.2. Observations and Reductions

NIR spectroscopy was obtained on three separate dates: on 2017 October 29 using Keck II NIRSPEC (McLean et al. 1998) and on 2018 October 25 and 2019 January 25 with Keck II Near-Infrared Echellette Spectrometer (NIRES; Wilson et al. 2004). NIRSPEC is a NIR echelle spectrograph with a wavelength coverage ranging from 0.9–5.5 μm. The NIRSPEC-7 filter was used in low-resolution mode with a cross-dispersion angle of 35.31°. This resulted in a wavelength coverage of ∼1.97–2.39 μm. The $42'' \times 0.76''$ slit was used, and a spectral resolution of 196 km s^{-1} ($R \approx 1500$) at 2.20 μm was measured with a seeing of $\sim 0.50''$. Observations throughout the night were done under mostly clear conditions. Note that these observations were done before the NIRSPEC upgrade. NIRES is an NIR echelette spectrograph with the slit being $18'' \times 0.55''$, and the wavelength coverage set from 0.94–2.45 μm across 5 orders. There is a small gap in coverage between 1.85 and 1.88 μm, but this is a region of low atmospheric transmission. The average spectral resolution of the 5 orders range between 84 and 89 km s^{-1} ($R \approx 3400$), and these differ less than 5% for each galaxy. Observations on 2018 October 25 were taken under variable and heavy cloud cover, however, the majority of our sample was observed on 2019 January 25, where cloud cover was light. Individual exposures for all sets of observations were 4 minutes each and were done using the standard ABBA nodding. A telluric standard star, typically of A0 spectral class with measured magnitudes in J, H, and K bands, was observed either directly before or after the target galaxy to correct for the atmospheric absorption features. Typical airmass differences with the target were below 0.10. A summary of the NIR observations is shown in Table 1.

In addition to the Keck NIRES and LRIS observations, follow-up optical integral field unit (IFU) observations with Keck Cosmic Web Imager (KCWI; Morrissey et al. 2018) and Gemini Multi-Object Spectrographs (GMOS; Allington-Smith et al. 2002; Gimeno et al. 2016) were done to obtain high spatial resolution of the outflows. The details of this analysis are discussed in L20.

Four of our targets (J0811+2328, J0906+5610, J0954+4717, and J1005+1257) were observed with the Chandra X-ray Observatory. Baldassare et al. (2017) report hard X-ray emission that is likely originating from the AGNs in J0906+5610 and J0954+4717. Additionally, Wang et al. (2016) provide fluxes, corrected for galactic absorption, for J0811+2328 and J1005+1257, from which we calculated a luminosity using the cosmology listed above. We discuss these results in Section 4.1.

The data were reduced using two modified pipelines. The first provided flat fielding and a robust background subtraction by using the techniques described in Kelson (2003) and Becker et al. (2009). In short, this routine maps the 2D science frame

and models the sky background before rectification thus reducing the possibility of artifacts appearing due to the binning of sharp features. The sky subtraction attained with this procedure is excellent despite the strong OH lines present in the NIR; the procedure is also quite insensitive to cosmic rays and hot pixels and is reliable regardless of skyline intensity.

Rectification, telluric correction, wavelength calibration, and extraction were all done with a slightly modified version of REDSPEC.[4] Telluric correction was done by dividing by the spectrum of the telluric standard star and multiplying by a blackbody curve of the same temperature. Strong OH skylines were used for wavelength calibration, and the 1D spectra were then median combined. Flux calibration of individual exposures was done using the telluric star and the Spitzer Science Center unit converter[5] to convert the magnitude of the star to the associated flux in that band. A small corrective factor (<5%) was introduced due to the differences between the center NIR bands and that of the wavelength coverage.

3. Analysis

3.1. Spectral Fitting

3.1.1. NIR Fitting

We fit all NIR spectra using EMCEE, an affine invariant Markov Chain Monte Carlo (MCMC) ensemble sampler (Foreman-Mackey et al. 2013). A narrow Gaussian component, along with a second order polynomial for the continuum, were fit simultaneously for each emission line. We determined whether a second Gaussian component was needed to fit the emission lines using the following F-test: $F = (\sigma_{\rm single})^2/(\sigma_{\rm double})^2$, where σ is the standard deviation of the residuals using either single or double Gaussian components. If $F > 2.0$, then adding an extra component is justifiable, and we added a component that is constrained to be broader and lower in amplitude than the first component to avoid degeneracies (see the Appendix for example figures). Both the narrow and broad components were treated as Gaussians with the amplitude, FWHM, and velocity offset from the rest-frame wavelength as free variables. We list all detected emission line fluxes and widths in the Appendix. Note that we only report 2σ detections and those with an FWHM greater than the resolution element.

As discussed in Section 4.1, we also use NIR absorption features in our analysis. These were also fit with MCMC in a similar fashion, the main difference being the amplitude was restricted to be negative. The fitting was done simultaneously with that of emission lines in order to keep the continuum level consistent across all measurements. Although we ran the F-test as defined above, only one Gaussian was needed for all the absorption fits. The widths and depth of the absorption features used in our analysis are also listed in the Appendix.

3.1.2. Sloan Digital Sky Survey Fitting

Sloan Digital Sky Survey Fitting (SDSS) spectra are available for our entire sample, and these provide full wavelength coverage from 4000–9000 Å, which includes the [O II] $\lambda\lambda$ 7320, 7330 doublet that is outside the LRIS coverage. The SDSS spectra were fit using Bayesian AGN Decomposition Analysis for SDSS Spectra (BADASS[6]; Sexton et al. 2021) a spectral analysis tool that fits the stellar and Fe II features. Absorption features were fit using the penalized Pixel Fitting (PPXF;[7] Cappellari & Emsellem 2004) method, and Fe II emission was fit using Fe II templates. All of these components were fit simultaneously, allowing for a detailed and robust analysis of the spectrum.

The code allows the user to test for the presence of outflows by setting various constraints on parameters such as minimum amplitude, minimum width, and velocity offset. The profile of [O III] λ5007 is often used as a tracer of outflows since it is isolated and in a region free of significant absorption. Through [O III] λ5007, we detected strong outflows in the SDSS spectra of six galaxies: J0100-0110, J0811+2328, J0842+0319, J0906+5610, J0954+4717, and J1005+1257 at a >95% confidence based on the F-test model comparison included in the code. J1009+2656 is a little more uncertain with a 89% confidence. We do not detect outflows (confidence <55%) for J0840+1818 and J1442+2054 likely due to the lower resolution of SDSS. These results are consistent with the KCWI results from L20 who found outflows in all targets but J0840+1818 (note that J1442+2054 was not observed with KCWI).

Table 2
Measured Extinction Values of the Sample

Galaxy	H α/Hβ Balmer Decrement	$E(B-V)$
J0100-0110	3.47 ± 0.27	0.115
J0811+2328	3.71 ± 0.34	0.182
J0840+1818	3.06 ± 0.17	0.000
J0842+0319	3.03 ± 0.14	0.000
J0906+5610	2.94 ± 0.18	0.000
J0954+4717	3.25 ± 0.08	0.049
J1005+1257	5.75 ± 0.27	0.624
J1009+2656	3.65 ± 0.10	0.166
J1442+2054	3.69 ± 0.15	0.176

Note. An intrinsic ratio of Hα/H$\beta = 3.1$ and a Cardelli reddening law were used.

3.2. Extinction

We note that L20 reports extinction values calculated from the Hγ/Hβ Balmer decrement. However, for J0100-0110 and J0811+2328, they used Hα/Hβ measurements from SDSS due to weak Hγ emission in their spectra. In addition, they did not observe J1442+2054. We thus opted to use the Hα/Hβ Balmer decrement measured from SDSS for our entire sample.

To quantify the extinction, we used the intrinsic line ratio of Hα/H$\beta = 3.1$, typically used for AGNs (e.g., VO87; Osterbrock et al. 1992), and a Cardelli reddening law (Cardelli et al. 1989) with an extinction factor of $R_V = 3.1$. We used the narrow-line flux measurements from the SDSS data (see Section 3.1.2), where we have decomposed the Hα and Hβ emission into narrow and broad (outflow) components. For the two galaxies, J0840+1818 and J1442+2054, where no outflow component was detected, we used the full emission line to obtain a flux. These values of the Balmer decrement and $E(B-V)$ for each galaxy are listed in Table 2, and all flux values in the Appendix reflect extinction-corrected fluxes. Note that three galaxies, J0840+1818, J0842+0319, and J0906

[4] https://www2.keck.hawaii.edu/inst/nirspec/redspec.html
[5] http://ssc.spitzer.caltech.edu/warmmission/propkit/pet/magtojy/
[6] https://github.com/remingtonsexton/BADASS2
[7] https://www-astro.physics.ox.ac.uk/~mxc/software/

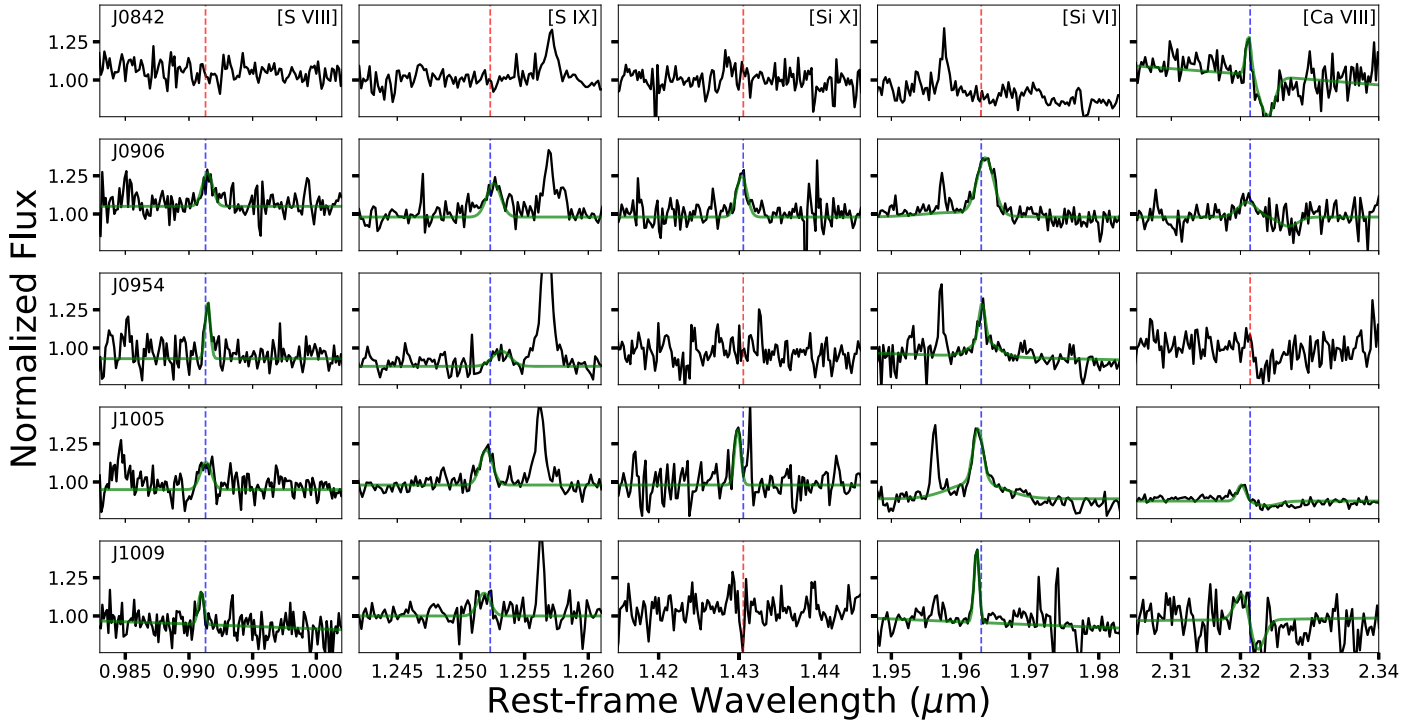

Figure 1. Zoom-in plots of the spectral regions around the most prominent NIR CLs, where the flux has been normalized to unity and the systemic redshift was used to shift the spectra to rest-frame wavelength. Dotted blue (detections) and red (non-detections) indicate the rest-frame wavelength of CLs. MCMC fits to the emission and absorption line profiles are shown as solid green lines.

+5610, have Balmer decrements slightly below the intrinsic ratio so we did not apply any extinction correction to them.

Our results are slightly different but generally agree with those calculated by L20. The discrepancies are likely caused by the different line ratios (Hγ/Hβ versus Hα/Hβ) and line profiles used, where we only used the narrow profile while L20 used the full (narrow + broad) profile. When comparing the effect of these two methods, the difference in flux measurements amounts to <5% for the majority of our sample. For the rest of this article, we use these extinction-corrected flux values unless otherwise specified.

3.3. CL Detections

55% (5/9) of our sample have NIR CL emission within the spectral window of 0.94–2.45 μm (see Table 1). For a similar spectral window and galaxy type, Sy1 and Sy2, this rate is consistent with others found in the literature: 66% (36 out of 54, Rodríguez-Ardila et al. 2011), 25% (5 out of 20, Mason et al. 2015), and 43% (44 out of 102, Lamperti et al. 2017). Our detections predominately come from sulfur and silicon species: [S VIII] 0.9913 μm, [S IX] 1.2523 μm, [Si X] 1.4305 μm, and [Si VI] 1.9630 μm. We also detect [Ca VIII] 2.3214 μm but it falls within the CO(3-1) absorption band at 2.3226 μm, making their measurements more uncertain. All of the detected NIR CLs are shown in Figure 1, where we include our MCMC fits to the emission line profiles. We do not detect other common NIR CLs such as [Fe XIII] 1.0747 μm, [S XI] 1.9196 μm, and [Al IX] 2.0450 μm. The most prominent CL is [Si VI] and is detected in four of the five galaxies with CL detections. This is not surprising since it has a lower ionization potential (IP) level than other CLs and is not near any absorption features. In three of these four galaxies, we find broad [Si VI] emission and thus use a two-component fit to the profile in accordance with the

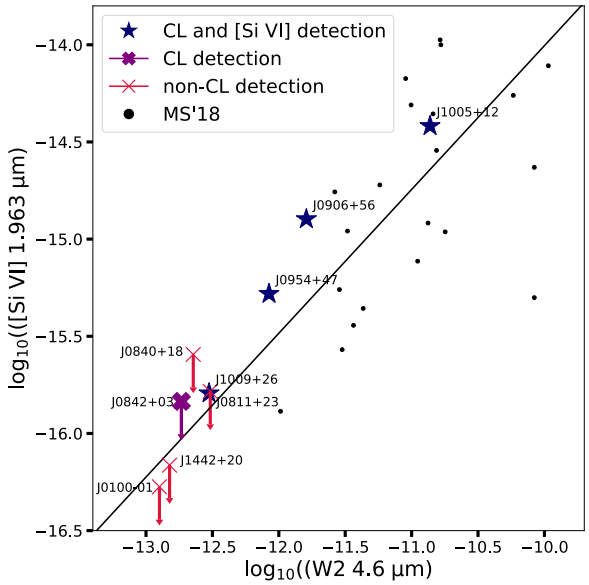

Figure 2. [Si VI] flux vs. W2 (4.6 μm) flux. Galaxies in our sample with detected [Si VI] emission are shown as blue stars. J0842+0319, the one object with a CL detection but no [Si VI] emission, is shown as a purple cross. Objects without any CL detections are shown as red crosses. For these latter two, the crosses represent 3σ upper limit fluxes to [Si VI]. The solid line is the best-fit line to the data found in Müller-Sánchez et al. (2018).

F-test mentioned in Section 3.1.1. Details of the multi-component fits to [Si VI] and plots of the entire spectra are presented in the Appendix.

No NIR CL emission is detected in the other four galaxies. To investigate this, we plotted total [Si VI] flux versus Wide-field Infrared Survey Explorer (WISE) W2 (4.6 μm) flux in Figure 2. Note that one galaxy, J0842+0319, has a CL

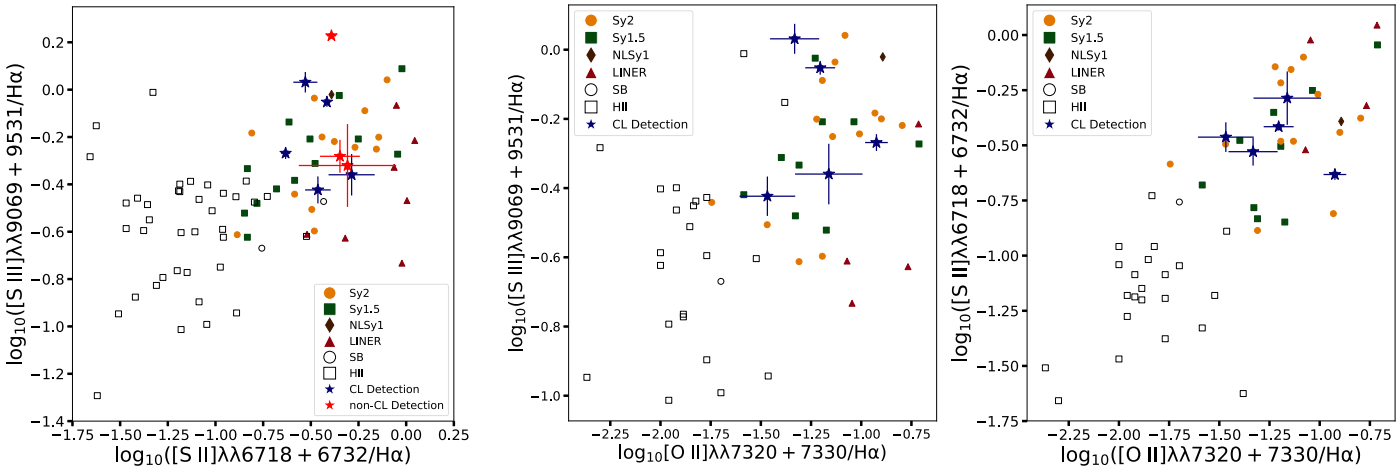

Figure 3. AGN diagnostic plots derived by Osterbrock et al. (1992). We plot our sample as blue (CL detection) and red (non-CL detection) stars. Our sample falls within the scatter of other galaxies hosting AGNs, further confirming the presence of AGNs.

detection, [Ca VIII], but does not show any [Si VI] emission. Upper limit fluxes to the non-[Si VI] detections were calculated by integrating over a Gaussian with a width equaling the resolution element and amplitude equaling the 1σ noise level where [Si VI] should appear. This value was multiplied by three to obtain the 3σ upper limit that is plotted in Figure 2. We also plot the AGN sample (black dots) from Müller-Sánchez et al. (2018) from which we derive the plotted line of best fit. This relation (J. Cann 2021, private communication) provides an expected value for [Si VI] based on W2 flux. Our non-detections lie below most of our [Si VI] measurements, suggesting that deeper observations may be required to detect any CL emission. Further discussion of our non-detections is covered in Section 4.1.

The optical data also reveal a number of CLs, particularly in those with NIR CL detections. 55% (5/9) of our sample have strong optical CL emission. The most common detections in our sample include [Ne V] λ3426, [Fe VII] λ6087, and [Fe X] λ6374. Less common lines include [Ne V] λ3346 and [Fe VII] λ5721. Most galaxies that have NIR CL emission also have optical CL emission, and the only exceptions are J0840+1818 and J0842+0319, where the latter only shows NIR CL emission. For J0840+1818, MK19 reported the detection of [Ne V] λ3426 but we do not find any NIR CLs. No other significant detections are seen in the rest of the sample. Additional details for each galaxy are covered in the Appendix. For the remainder of this article, we label galaxies as either having NIR CL emission or not.

3.4. AGN Diagnostic Plots

Although there is evidence for AGN activity in our dwarf galaxy sample, including optical BPT/VO87 AGN line ratios, the addition of NIR lines allows us to run additional AGN diagnostics. With the inclusion of [S III] λ9531, we can test our sample with the AGN diagnostics presented in Osterbrock et al. (1992). Specifically, we use the [S III] $\lambda\lambda$ 9069+9531/Hα versus [S II] $\lambda\lambda$ 6718+6732/Hα, [S III] $\lambda\lambda$ 9069+9531/Hα versus [O II] $\lambda\lambda$ 7320+7330/Hα, and [S II] $\lambda\lambda$ 6718+6732/Hα versus [O II] $\lambda\lambda$ 7320+7330/Hα (their Figures 4, 5, and 7). All three of these relations are plotted in Figure 3, where we include the AGNs and star-forming samples from Osterbrock et al. (1992). We overplot narrow-line fluxes of our sample as stars and exclude the galaxies with no measurable [O II] $\lambda\lambda$ 7320, 7330. J0100-0110 is also omitted since its [S III] λ9531 is outside the wavelength coverage of NIRSPEC. Since [S III] λ9069 is outside the wavelength coverage of NIRES, we use the intrinsic flux ratio of [S III] $\lambda 9531/\lambda 9069 = 2.6$ to obtain flux values for [S III] λ9069.

In all three relations, our dwarf sample falls within the scatter of the AGN sample in Osterbrock et al. (1992). As discussed in Section 3.3, not every galaxy in our sample show CLs. To check if this has any effect, we separate our sample into two groups: those with CL emission and those without. We find that they all lie in similar regions and we see no clear distinction between them in all three relations. While no single line ratio can confidently separate AGN activity from star formation, our dwarf sample shows optical and NIR line ratios that, when considered collectively, strongly suggest the presence of AGNs.

4. Discussion

4.1. Detection Rate of CLs

Although CLs are excellent tracers of AGN activity, they do not always appear in AGN spectra and a number of reasons have been proposed to explain this. In general, CL detections decrease with increasing IP and our results agree with this; we do not detect any of the high-IP CLs, [Fe XIII] 1.0747 μm (330.8 eV) and [S XI] 1.9196 μm (447.1 eV). Stellar absorption features can also affect detection rates by attenuating the CL emission profile. Such is the case with [Ca VIII], which falls within the CO (3-1) absorption feature. In addition, Ca and Al species can be affected by metallicity and depletion onto dust. Moreover, telluric absorption from the atmosphere always has to be contended within ground-based observations.

In nearby low-luminosity AGNs, circumnuclear stellar populations can dominate the NIR continuum and thus drown out any CL emission. Bright AGNs, particularly at high redshift, can also hamper CL emission due to their strong continuum. These effects can be seen in the results of Rodríguez-Ardila et al. (2011) who found that many galaxies with stars contributing $\sim$90% of the continuum do not show CL emission. They also found their CL detection rate decreased by 17% when selecting galaxies with a redshift $>$0.05.

Our coverage of J, H, and K bands allows us to estimate the contribution of circumnuclear stellar populations. The CO(6-3)

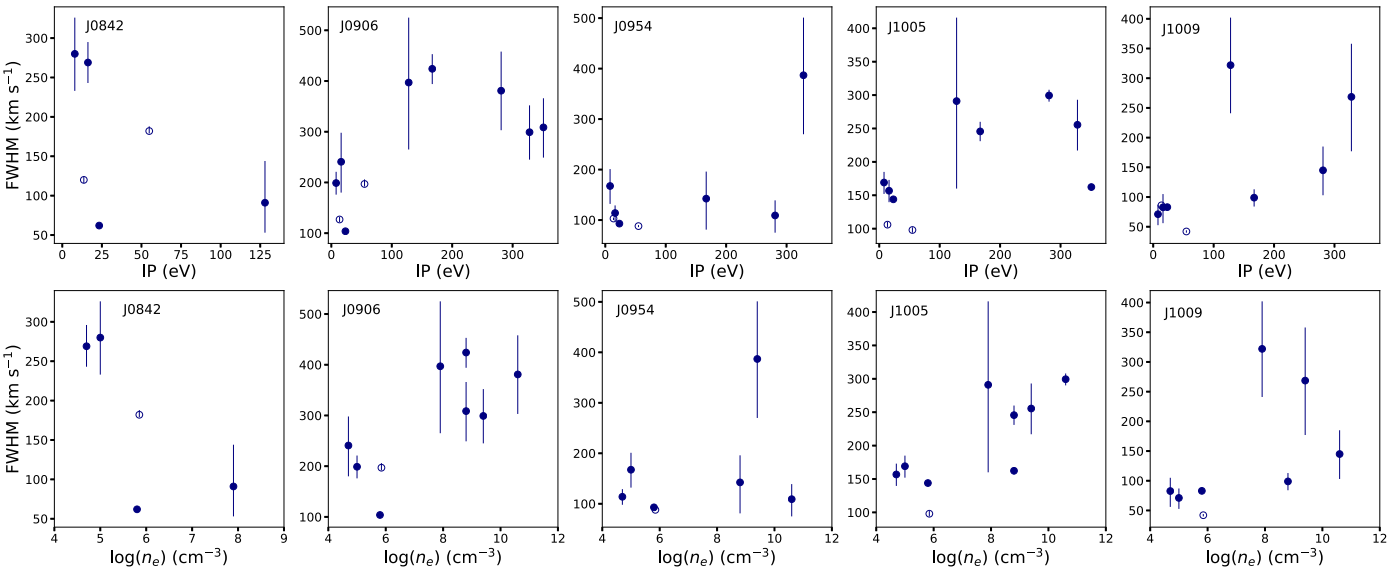

Figure 4. FWHM vs. IP (top panels) and critical density (bottom panels) for our sample with NIR CL detections. Low-ionization optical emission lines are plotted as open circles, while all NIR emission lines are plotted as filled circles.

Table 3
Emission Lines with IP and Critical Densities

Emission Line (μm)	IP (eV)	log(n_e) (cm^{-3})	Emission Line (μm)	IP (eV)	log(n_e) (cm^{-3})
Hα	13.6	⋯	[Fe II]1.2567	7.9	5.0
[O III]0.5007	54.9	5.85	[Si X]1.4305	351.1	8.8
[S III]0.9531	23.3	5.8	[Fe II]1.6435	16.2	4.7
[S VIII]0.9913	280.9	10.6	[Si VI]1.9630	166.8	8.8
[Si IX]1.2523	328.2	9.4	[Ca VIII]2.3214	127.7	7.9

absorption at 1.62 μm can provide an estimate to the flux contribution of red giants to the *H*-band continuum (Martins et al. 2010), where the continuum level arises due to stellar and AGN contribution. For a population of GKM giants, the typical observed depth of the absorption is ∼20% of the continuum (Schinnerer et al. 1998). Our sample ranges from 7%–14% (median of 11%), suggesting a large contribution to the *H*-band continuum from red giants, up to 70%. The weighted average of the depth of galaxies with no CL detections is 28% deeper than those with CL emission. One possibility is that a larger population of red giants near the center could be the cause of the deeper absorption and are thus directly increasing the continuum level. Alternatively, a shallower CO absorption may be indicative of a stronger AGN contribution to the continuum, which would likely lead to stronger CL emission that is more easily detectable.

Baldassare et al. (2017) reported 0.5–7 keV X-ray luminosities for J0906+5610 and J0954+4717, from which we convert to $L_{2-10\,\mathrm{keV}}$ using the Portable, Interactive Multi-Mission Simulator.[8] This results in a $L_{2-10\,\mathrm{keV}}$ of 2.89×10^{40} erg s^{-1} and 6.12×10^{39} erg s^{-1} for J0906+5610 and J0954+4717, respectively. Additionally, using 0.3–8 keV fluxes from Wang et al. (2016), we calculated 2–10 keV luminosities for J0811+2328 (1.33×10^{39} erg s^{-1}) and J1005+1257 (5.20×10^{39} erg s^{-1}). Although J0811+2328 does have the lowest X-ray luminosity, we find no clear distinctions between galaxies with CL detections and those without. We do note, however, that these X-ray luminosities are about 2 orders of magnitude lower than the $L_{2-10\,\mathrm{keV}}$–L_{W2} relation discussed in Secrest et al. (2015). Indeed, all four targets have $L_{2-10\,\mathrm{keV}}/L_{W2} < -2.1$. Similar low L_X have been reported in low-mass galaxies (Dong et al. 2012; Simmonds et al. 2016; Cann et al. 2020), suggesting obscuration of the X-ray source emission or that AGNs in dwarf galaxies are X-ray weak compared to their mid-IR emission.

4.2. CL and Outflow Kinematics

Photoionization is widely considered as the main excitation mechanism behind CL emission, although Rodríguez-Ardila et al. (2006) found that their models more precisely matched emission line ratios from their data when shocks were included. If, however, photoionization is the principle excitation mechanism behind CLs, then we expect a correlation between the FWHM and IP. Emission from a high-IP line would suggest that the emitting gas is located closer to the central ionizing source and thus be deeper in the gravitational well, causing a broadening of its emission line profile. Because of their high range of IPs (∼100–500 eV), CLs are ideal in investigating the gas kinematics near the AGNs. Indeed, positive correlations between line width and IP have been found in past studies (e.g., De Robertis & Osterbrock 1984; De Robertis & Shaw 1990; Veilleux 1991a) for optical high ionization lines. A positive trend has also been found between line width and critical density in these studies. Similar trends between line width and IP for NIR lines have been seen in some galaxies (Rodríguez-Ardila et al. 2002), but larger samples are starting to show more varied CL widths (e.g., Rodríguez-Ardila et al. 2011; Villar Martín et al. 2015; Cerqueira-Campos et al. 2021), and in many cases no trends are found at all. Rodríguez-Ardila et al. (2011) found a positive slope up to ∼300 eV, after which the slope turned negative (i.e., higher IP, lower FWHM). They attribute this to the increase in electron density when approaching the central AGNs. Due to densities exceeding the critical densities of the high-IP CL ions, these lines may be suppressed. Specifically, collisional de-excitation could reduce emission associated with the broader, high velocity components, thus

[8] https://cxc.harvard.edu/toolkit/pimms.jsp

Table 4
Outflow Properties

Galaxy (1)	[O III] Component (2)	[O III] v_{50} (km s^{-1}) (3)	[Si VI] v_{50} (km s^{-1}) (4)	[O III] W_{80} (v_{out}) (km s^{-1}) (5)	[Si VI] W_{80} (v_{out}) (km s^{-1}) (6)	log($L_{[Si\ VI]}$) (erg s^{-1}) (7)	log(L_{AGN}) (erg s^{-1}) (8)
J0100-0110	Total	−130	⋯	440 (350)	⋯	<38.49	43.3
	C1	−60	⋯	210 (165)	⋯	⋯	
	C2	−240	⋯	650 (565)	⋯	⋯	
J0811+2328	C1	−60	⋯	220 (170)	⋯	<37.95	41.8
J0840+1818	C1	−30	⋯	130 (95)	⋯	<38.10	41.9
J0842+0319	Total	−110	⋯	700 (460)	⋯	<38.42	42.7
	C1	−60	⋯	220 (170)	⋯	⋯	
	C2	−160	⋯	750 (535)	⋯	⋯	
J0906+5610	Total	−50	90, −600	670 (385)	970 (535)	42.48	43.3
	C1	−50	⋯	140 (120)	⋯	⋯	
	C2	30	⋯	680 (310)	⋯	⋯	
	C3	−150	⋯	1250 (775)	⋯	⋯	
J0954+4717	Total	−10	17, 60	530 (275)	650 (300)	42.09	43.6
	C1	0	⋯	100 (50)	⋯	⋯	
	C2	−70	⋯	430 (285)	⋯	⋯	
	C3	−80	⋯	1100 (630)	⋯	⋯	
J1005+1257	Total	−60	−70, −100	680 (400)	1350 (770)	43.04	43.2
	C1	−40	⋯	120 (100)	⋯	⋯	
	C2	−100	⋯	710 (455)	⋯	⋯	
	C3	−200	⋯	1200 (800)	⋯	⋯	
J1009+2656	Total	−50	−100	150 (125)	108 (155)	41.59	42.9
	C1	−30	⋯	100 (80)	⋯	⋯	
	C2	−60	⋯	480 (300)	⋯	⋯	

Note. Columns: (1) Galaxy name. (2) Components of the [O III] fit according to L20. In general, the C3 component traces the faster, broader outflow component while C2 traces the more narrow outflow component. C1 generally traces the gas of the narrow-line region. (3) Minimum values (i.e., maximum blue offset from the systemic velocity) of v_{50} based on [O III] λ5007 measurements from L20. (4) v_{50} values for [Si VI]. The first value is for the narrow component, followed by the broad component. (5) Maximum W_{80} values based on [O III] λ5007 measurements from L20. In parentheses are v_{out} values as defined in Equation (1). (6) W_{80} of the outflow based on the full [Si VI] profile. v_{out} values are in parentheses. (7) Total luminosity of [Si VI]. Upper limits are included for galaxies without [Si VI] detections (see Section 3.3 for details). (8) Extinction-corrected AGN luminosity as derived from [O III] λ5007 in L20. Extinction values used were derived in this article.

causing us to only see the narrow emission and explaining the decrease in the FWHM at high IPs.

We run a similar analysis by plotting a narrow-component FWHM versus IP and critical density for the CLs detected in our sample in Figure 4. We have also included optical (open circles) and NIR low-ionization lines to draw comparisons (see Table 3). In two galaxies, J0906+5610 and J1005+1257, the widths peak around 250–300 eV and subsequently decrease, consistent with collisional de-excitation of the broader components of high-IP ions. The CL emission in the other three galaxies have a lower S/N so it is difficult to evaluate any trends. Aside from these low S/N measurements (as indicated by their error bars), these CLs have widths consistent with the lower IP lines. However, some uncertainty may arise from overestimating/underestimating the broad/narrow component of the line profile. For instance, the relatively small width of [Si VI] (166.8 eV) in J0954+4717, where we have added a secondary broad component, could be due to overestimating the broad component. Regardless, our results are consistent with the recent reports finding no clear trends between the FWHM and IP.

Critical density, defined as the density when the collision rate matches the radiative de-excitation rate, is plotted against the FWHM in the bottom panels of Figure 4. Consistent with past works (De Robertis & Osterbrock 1986; Veilleux 1991b; Ferguson et al. 1997), we find linear correlation in some galaxies with varying degrees of slope. Regardless, we find a stronger correlation of the FWHM increasing with critical density, consistent with past studies.

Table 4 lists the kinematic properties of the narrow and broad (outflow) components of [O III] and [Si VI], where the [O III] values come from L20. The higher spectral resolution of the IFU data of L20 allowed for the decomposition of the emission line profile into two or three components. Generally, the C1 component traces the gas in the narrow-line region, while C2 and C3 represent the broader and bluer components to the multicomponent fit and thus likely trace the outflow. For J0811+2328, only one component (C1) was fit but it is blueshifted relative to the stellar velocity and broader than the stellar velocity dispersion, and thus L20 suggested that it is likely part of the outflow. For v_{50}, the median velocity offset of the profile relative to systemic velocity, we take the minimum values (i.e., maximum blue offset) for [O III].

The velocity of an outflow is often calculated through the use of W_{80}, the width containing 80% of the flux of an emission line (Harrison et al. 2014). For a single Gaussian profile, $W_{80} = 1.09 \times \mathrm{FWHM}$. To measure W_{80} for [Si VI] , we use the full profile due to the relatively large uncertainties in the broad component. We can define the outflow velocity as

$$v_{out} = -v_{50} + \frac{W_{80}}{2}. \quad (1)$$

Although C1 likely traces the narrow-line gas, L20 and Manzano-King & Canalizo (2020, hereafter MC20) found cases where outflowing gas can be represented as a single-component profile. For this reason, we include v_{out} calculations for all [O III] components. In addition, for [Si VI] v_{out}, we use v_{50} of the full profile if a multicomponent fit was used. This is

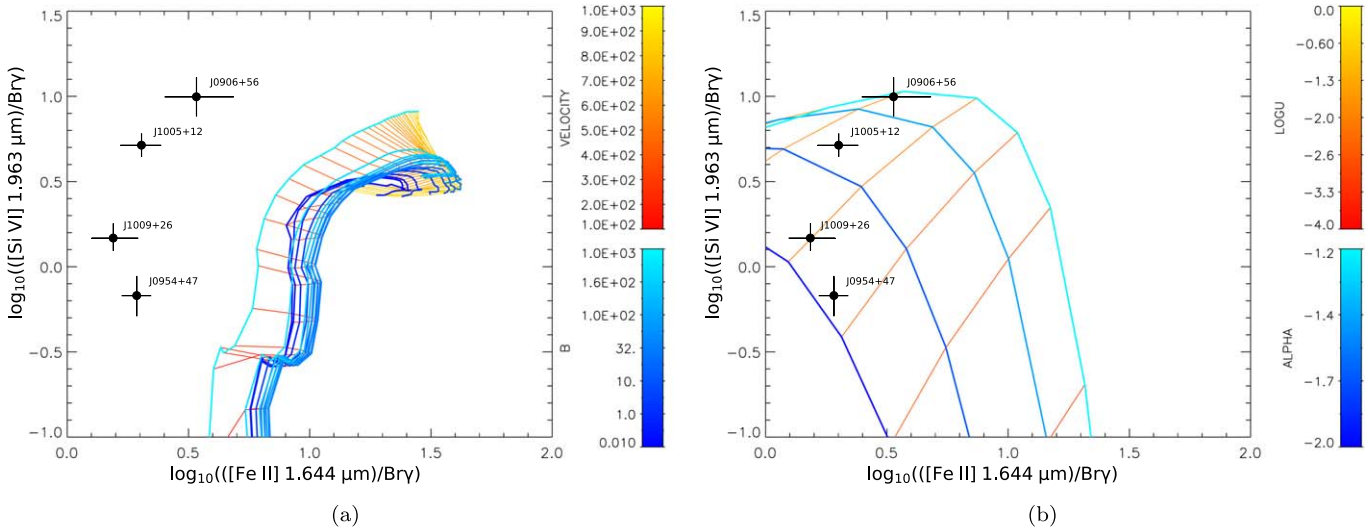

Figure 5. Log_{10}([Si VI]/Brγ) vs. $\log_{10}$(Fe II/Brγ) for (a) shock + precursor and (b) AGN model plots. Free parameters for the shock + precursor grid lines are the shock velocity v_{shock} and magnetic field parameter B. Free parameters for the AGN grid lines are the power-law index α and the ionization parameter U. The four galaxies with detected [Si VI] emission are plotted as black circles with error bars. Metallicity was set to solar and a gas density of $n = 1000$ cm^{-3} was assumed.

Table 5
J0100 NIR Emission Line Parameters

Emission	FWHM (km s^{-1})	Flux (10^{-17} erg cm^{-2} s^{-1})	Notes
Paα 1.8756 μm	62 ± 7	141 ± 6	Edge of wavelength coverage
Brγ 2.1661 μm	97 ± 46	11 ± 1	

Note. Only NIRSPEC (K-band) observations were done. Columns: (1) Emission line. (2) FWHM of the emission line and its error after instrument correction. Uncertainties are only representative of random error in the fit. (3) Flux and error of the emission line, where uncertainties are from random errors. (4) Notes regarding the fitting.

because of the large uncertainties associated with the broad component fits.

Our data show the outflow velocities seen in [Si VI], measured through either W_{80} or v_{out}, are generally faster than those seen in [O III]. The main exception to this are the velocities seen in the C3 components. This is likely due to combining the narrow and broad components of [Si VI] when calculating W_{80} and v_{50}. Using only the broad component, we find velocities to be consistent or higher than those of C3, albeit with much higher uncertainty. This overall trend of higher velocities seen in [Si VI] than in [O III] implies a decelerating outflow, one where a high velocity wind originates near the AGNs and slows down as it approaches the outer, lower ionization gas.

We also note that the objects with the fastest outflows and broadest profiles seen in [O III], J0906+5610, J0954+4717, and J1005+1257, have the broadest [Si VI] emission. This is perhaps unsurprising since we are observing the same outflow, just at different locations.

We also list the bolometric AGN luminosities (L_{AGN}) in Table 4. These values were derived from the observed [O III] λ5007 flux in L20. Empirical bolometric correlation factors from Lamastra et al. (2009) were used: $L_{\mathrm{AGN}} = 87\ L_{[\mathrm{O\ III}]}$ for $38 < \log(L_{[\mathrm{O\ III}]}) < 40$ and $L_{\mathrm{AGN}} = 142\ L_{[\mathrm{O\ III}]}$ for $40 < \log(L_{[\mathrm{O\ III}]}) < 42$. To correct for extinction, we applied the extinction values listed in Table 2. We find no strong correlation between AGN luminosity and outflow speeds, but there is a trend for the more luminous AGNs to have a higher number and more luminous CL detections. If we assume a simple biconical outflow starting close to the AGNs (for a detailed analysis, see Müller-Sánchez et al. 2011), highly ionized gas (i.e., CLs) could more easily be sent out to farther, possibly less obscured regions due to a fast outflow. Although it is difficult to make any firm conclusions due to the CL region being unresolved in our data, it appears that faster outflows may result in stronger and broader CL emission.

4.3. Ionization and Origin of the Outflows

In this section, we investigate whether AGNs or stellar processes (or both) are the primary source of ionization and the driving mechanism for the outflows.

4.3.1. AGNs or Stellar Ionization?

The analysis of line ratios by L20 indicates that AGNs are the primary source of ionization in our sample. However, they note that ionization from shocks, possibly originating from starburst driven winds (Sharp & Bland-Hawthorn 2010), cannot be ruled out. To investigate this further, we compare line ratios in our sample to ionization models found in the literature. Riffel et al. (2013) and Colina et al. (2015) plot [Fe II] 1.64 μm/Brγ versus H_2 2.12 μm/Brγ to separate AGNs from star-forming samples. However, the five galaxies with obtainable line ratios fall within the overlap between the AGN and SNe-dominated distributions (see Figure 5 from Colina et al. 2015). We instead use the flux ratios of [Si VI]/Brγ and [Fe II] 1.64 μm/Brγ, where [Fe II] is a sensitive indicator of shocks (U et al. 2013) and Brγ serves as an indicator of stellar activity and the ionizing radiation field. We compare these ratios to the AGN ionization models from Groves et al. (2004a, 2004b) and shock models from Allen et al. (2008). We extracted these models from the IDL Tool for Emission-line Ratio Analysis library (Groves & Allen 2010) and plotted them in Figure 5. The shock model (Figure 5, left) takes into account both the shocked gas and precursor gas, which lies ahead of the

shock front. Quick inspection of shock-only model (not plotted) shows a shift toward higher [Fe II]/Brγ ratios, farther away from our measured line ratios. We thus focus our analysis on the shock + precursor model (hereafter simply shock model) since the individual regions cannot be resolved in our data. Free parameters for the shock model include the shock velocity $v_{\rm shock}$ (10–1000 km s^{-1}) and the magnetic field parameter $B/n^{1/2}$ (10^{-4}–10 μG cm$^{3/2}$), where B is the transverse magnetic field. The AGN model free parameters include the power-law index α and the ionization parameter U, where $U \equiv n_{\rm ion}/n_{\rm e}$, $n_{\rm ion}$ is the density of the ionizing photons, and $n_{\rm e}$ is the electron density. The model uses a simple power law, $F_\nu \propto \nu^\alpha$, where $5\,{\rm eV} < \nu < 1000\,{\rm eV}$ (see Groves et al. 2004a, 2004b, for further details).

To estimate the CL gas density, Landt et al. (2015a, 2015b) used line ratios of the [Fe VII] $\lambda\lambda\lambda$3759, 5159, 6087 optical CLs. Although we do not detect all these lines in our optical data, some targets do have two [Fe VII] emission lines that are measurable. For these targets, we calculated an upper limit flux to the third [Fe VII] line and obtained a rough estimate of the gas density. These values are consistent with a density of 1000 cm^{-3}. In addition, L20 used the S II λ6716/S II λ6731 line ratio (e.g., Sanders et al. 2016) and obtained values of $\sim$500 cm^{-3} for most of their sample. They thus use a density of 1000 cm^{-3} in their models. Therefore, in both of our models, we use a gas density of 1000 cm^{-3}. Lastly, metallicity was set to solar.

We use the total flux for each emission line and plot the ratios over the shock model (Figure 5, left) and AGN model (Figure 5, right). It is clear that the line ratios are well within the AGN model parameters ($-2.0 \lesssim \alpha \lesssim -1.2$ and $-3.3 \lesssim \log(U) \lesssim -2.0$). As for the shock models, the line ratios are offset by more than 0.5 dex and all have systematically larger [Fe II]/Brγ ratios. In order to match the measured data, it appears a relatively large magnetic parameter ($>10^3$) is required. Thus, it is likely that AGNs are the dominant ionizing source in our sample, though a small contribution from shocks cannot be formally ruled out.

4.3.2. AGNs or Stellar Driven Winds?

The matter of identifying the driving force behind the outflows is a difficult but important issue to investigate. Outflowing winds are often cited coming from either AGN or starburst activity (e.g., Fabian 2012; Rupke 2018; Veilleux et al. 2020), though distinguishing between the two is often difficult. L20 investigated the energies associated with the outflows in our sample and found that the AGNs are more than powerful enough to drive them. However, they found that typical core-collapse SNe can also provide the necessary energy output needed.

One avenue of checking the likelihood of starburst driven winds in our sample is to estimate the age of a stellar population. The CN absorption features at 1.1 μm have been shown to serve as an indicator of an intermediate-aged stellar population (Maraston 2005; Riffel et al. 2007). This band most notably arises from carbon stars where there is an excess of carbon that is not bonded in CO molecules. To form a carbon star, a third "dredge-up" during the thermally pulsing asymptotic giant branch (TP-AGB) is necessary and this constrains the stellar population age to be within 0.3–2 Gyr. Thus, CN absorption would identify a younger to intermediate-aged stellar population and signify an occurrence of starburst activity.

The absence of CN absorption, however, may not necessarily imply an absence of a young to intermediate-aged stellar population. Riffel et al. (2009) and Martins et al. (2013) reported cases with no CN absorption but with known intermediate populations and vice versa. But as they pointed out, this is not to say that CN does not trace an intermediate population. Overlap with strong emission from He I 1.08 μm and Paγ can partially or fully obstruct the CN absorption. Telluric absorption, particularly in galaxies with low redshift ($z < 0.01$), may also interfere with CN detection. Even with proper correction from a telluric standard, the residuals can have substantial effects on the S/N on the CN features.

Visual inspection of our spectra shows no interference from strong emission lines but we do find significant telluric absorption in the region of CN in two cases (see the Appendix for more details). For the rest, this lack of CN absorption would indicate that much of the CO absorption comes from older red giants (see Section 4.1). This is also consistent with the stellar population age estimates of at least several gigayears modeled from optical LRIS spectra (Manzano-King 2020). This apparent deficit of young stars would suggest a lack of starburst that could drive the outflows we see, making the outflows more likely to be driven by AGNs.

5. Conclusion

We have presented Keck NIR spectroscopy of a sample of dwarf galaxies with strong evidence of AGN activity and have shown the outflows detected are likely AGN driven. Eight galaxies were observed with Keck NIRES, providing full wavelength coverage from 0.9–2.4 μm, and one galaxy with Keck NIRSPEC, with wavelength coverage from 1.97–2.39 μm. The main results are summarized below.

1. NIR CLs (IP > 100 eV) are detected in 5/9 (55%) galaxies in our sample, consistent with detection rates found in larger mass studies. Due to their high ionization potentials, CL emission is highly indicative of AGN activity. Coupled with optical and other NIR AGN diagnostics, there is strong evidence for AGN activity in these dwarf galaxies.
2. For the four galaxies without NIR CL emission, we suspect a strong contribution from a population of red giants that could be dominating the continuum level and hamper any weak CL emission. The deeper CO(6-3) absorption at 1.62 μm in these galaxies indicates a larger population of old stars. Alternatively, the deeper CO absorption may be indicative of weaker AGNs that would result in more elusive CL emission.
3. No clear trends are found between the widths of the CLs and their IPs. Two galaxies show a decrease in width after peaking around 250–300 eV. As noted in previous works, this is likely due to collisional de-excitation caused by the high density environments near the central ionizing source. In addition, we see a positive trend between the FWHM and the critical densities in these two galaxies. The other galaxies show CL widths that are consistent with lower IP lines and their widths are not as tightly correlated with critical densities.
4. The outflow velocities measured from [Si VI] emission are generally faster than those measured from [O III]. This

indicates the presence of a decelerating outflow. We also find that the galaxies with the highest [Si VI] luminosity also have the fastest outflows measured in [O III].

5. Examination of ionization models reveals that NIR emission line ratios of our sample are more consistent with AGN models than with shock + precursor models. This indicates that AGNs are the main ionizing source, though a smaller contribution from shocks cannot be formally dismissed.
6. The lack of CN absorption at 1.1 μm suggests a lack of young/intermediate (0.3–2.0 Gyr) circumnuclear stars in our sample. This goes against the scenario where the outflows are produced by starburst activity, suggesting AGNs as the main driving force of the outflows.

We thank the referee for their time and helpful comments on this work. We also thank Lisa Prato for her assistance with REDSPEC and George Becker for assisting with the NIR reduction pipeline.

We thank Dr. Percy Gomez and Dr. Sherry Yeh for supporting our Keck observations. Partial support for this project was provided by the National Science Foundation, under grant No. AST 1817233. S.V. and W.L. acknowledge partial support for this work provided by NASA through grants HST GO-15662.001A and GO-15915.001A from the Space Telescope Science Institute, which is operated by AURA, Inc., under NASA contract NAS 5-26555. We also thank Dr. Randy Campbell and the support provided by the Keck Visiting Scholars Program.

Some of the data presented herein were obtained at the W. M. Keck Observatory, which is operated as a scientific partnership among the California Institute of Technology, the University of California, and the National Aeronautics and Space Administration. The Observatory was made possible by the generous financial support of the W. M. Keck Foundation.

The authors wish to recognize and acknowledge the very significant cultural role and reverence that the summit of Maunakea has always had within the indigenous Hawaiian community. We are most fortunate to have the opportunity to conduct observations from this mountain.

Funding for the SDSSI/II has been provided by the Alfred P. Sloan Foundation, the participating institutions, the National Science Foundation, the U.S. Department of Energy, the National Aeronautics and Space Administration, the Japanese Monbukagakusho, the Max Planck Society, and the Higher Education Funding Council for England. The SDSS website is located at http://www.sdss.org/. The SDSS is managed by the Astrophysical Research Consortium for the Participating Institutions. The participating institutions are the American Museum of Natural History, Astrophysical Institute Potsdam, University of Basel, University of Cambridge, Case Western Reserve University, University of Chicago, Drexel University, Fermilab, The Institute for Advanced Study, the Japan Participation Group, Johns Hopkins University, The Joint Institute for Nuclear Astrophysics, the Kavli Institute for Particle Astrophysics and Cosmology, the Korean Scientist Group, the Chinese Academy of Sciences (LAMOST), Los Alamos National Laboratory, the Max Planck Institute for Astronomy (MPIA), the Max Planck Institute for Astrophysics (MPA), New Mexico State University, Ohio State University, University of Pittsburgh, University of Portsmouth, Princeton University, the United States Naval Observatory, and the University of Washington.

Software: BADASS (Sexton et al. 2021) https://github.com/remingtonsexton/BADASS2), PPXF (Peng et al. 2002, 2010), PYRAF (PyRAF is a product of the Space Telescope Science Institute, which is operated by AURA for NASA), REDSPEC (https://www2.keck.hawaii.edu/inst/nirspec/redspec.html).

Appendix
Details of CL Emission

In this section, we cover the NIR spectra in our sample of dwarf galaxies, with particular detail to the CL emission and important absorption bands. The following subsections are in order of increasing RA of the galaxy. In the figures showing the full wavelength coverage of our data, we provide subplots that give additional detail to key features, such as absorption features and emission lines (or lack thereof). The measured properties of every NIR emission line detected at the 3σ level are listed in Tables 5–13. The listed uncertainties come from the random error estimates during the fitting process.

A.1. J010005.92-011058.89

J0100-0110 is one of only two galaxies in the composite region of the BPT diagram. Based on optical emission line measurements, MC20 reported disturbed gas that is offset from the stellar rotation curve derived from a Navarro–Frenk–White dark matter density profile (Navarro et al. 1996). Indeed, L20 reported strong, blueshifted [O III] emission in the southern portion of J0100-0110, seen predominately in the C2 component. They suggested that this could be emission from the near side of a biconical outflow.

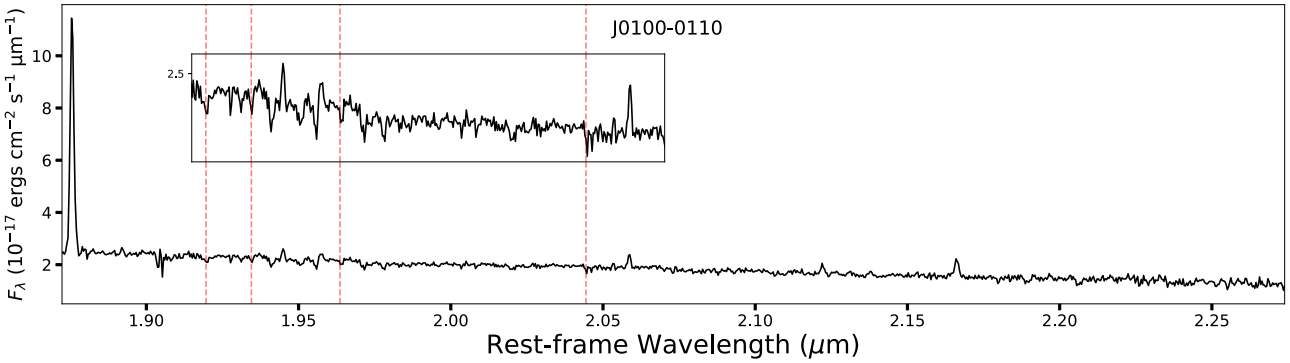

Figure 6. Spectrum of J0100-0110 taken with NIRSPEC, shifted to rest-frame wavelength using the systemic redshift. Red-dashed lines represent CLs that we do not detect at the 2σ level.

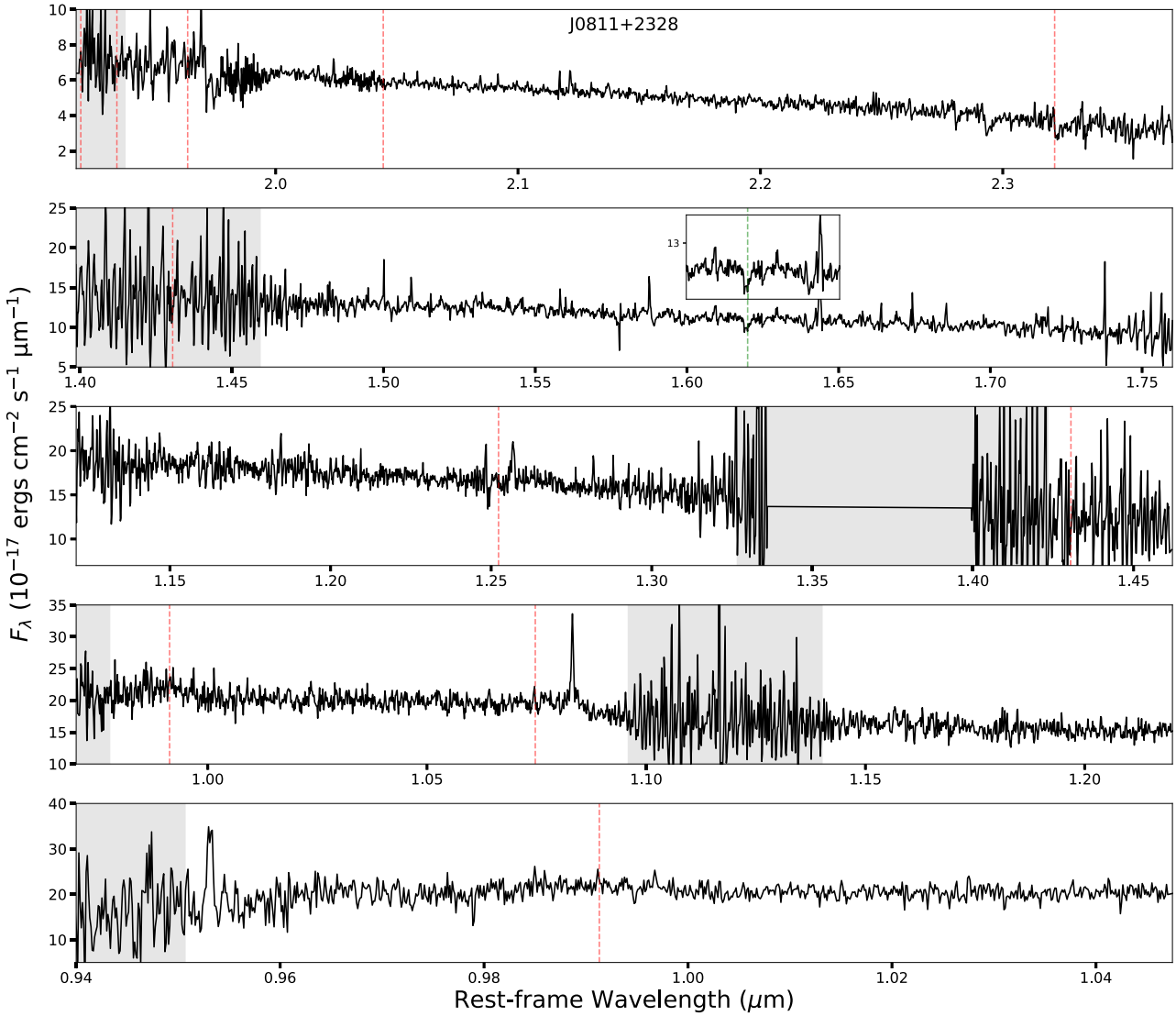

Figure 7. Spectrum of J0811+2328 taken with NIRES, shifted to rest-frame wavelength using the systemic redshift. Red- and green-dashed lines represent CLs that we do not detect at the 2σ level and the CO (6–3) absorption at 1.62 μm, respectively. The gray-shaded regions indicate areas of significant telluric absorption.

The NIR spectrum of J0100-0110 is shown in Figure 6 and line measurements are listed in Table 5. It is the only galaxy in our sample observed with NIRSPEC (wavelength coverage from ∼1.97–2.39 μm). Because of this, we cannot make estimates to the stellar age as we have done with the rest of the sample. The spectrum shows strong Paα and Brγ; it shows no CL emission in the *K* band. No significant optical CL emission is detected in this galaxy.

A.2. J081145.29+232825.72

Moran et al. (2014) reported a lower limit to the BH mass of $\log(M_{\rm BH}/M_\odot) > 4.4$ based on Eddington luminosity arguments. Wang et al. (2016) reported Chandra 0.3–8 keV flux, from which we calculate a 2–10 keV luminosity of 1.33×10^{39} erg s^{-1}. MC20 reported both disturbed and stratified gas in J0811+2328. Here, the gas is both offset from the stellar rotation curve, and the Balmer and forbidden lines are kinematically distinct from one another. In L20, only a single component was needed to fit the [O III] profile, but the larger line widths (relative to the velocity dispersion of the stellar

Table 6
J0811 NIR Emission Line Parameters

Emission	FWHM (km s^{-1})	Flux (10^{-17} erg cm^{-2} s^{-1})	Notes
[S III] 0.9531 μm	173 ± 9	153 ± 26	Low transmission
He I 1.0830 μm total	137 ± 16	98 ± 17	…
[Fe II] 1.2486 μm	19^{+42}_{-19}	21 ± 6	On skyline
[Fe II] 1.2567 μm	265 ± 44	61 ± 13	On skyline
Paβ 1.2822 μm	51 ± 48	19 ± 6	On skyline
[Fe II] 1.6435 μm	110 ± 19	39 ± 6	On skyline
H_2 2.1218 μm	66^{+32}_{-57}	11 ± 2	…
CO(6-3) 1.62 μm	386 ± 81	⋯	Absorption feature

Note. Same as Table 5. The CO(6-3) absorption feature at 1.62 μm is added at the bottom, along with the FWHM. The depth of the absorption feature measures about 13% of the continuum, suggesting roughly 65% of the *H*-band continuum comes from GMK red giants.

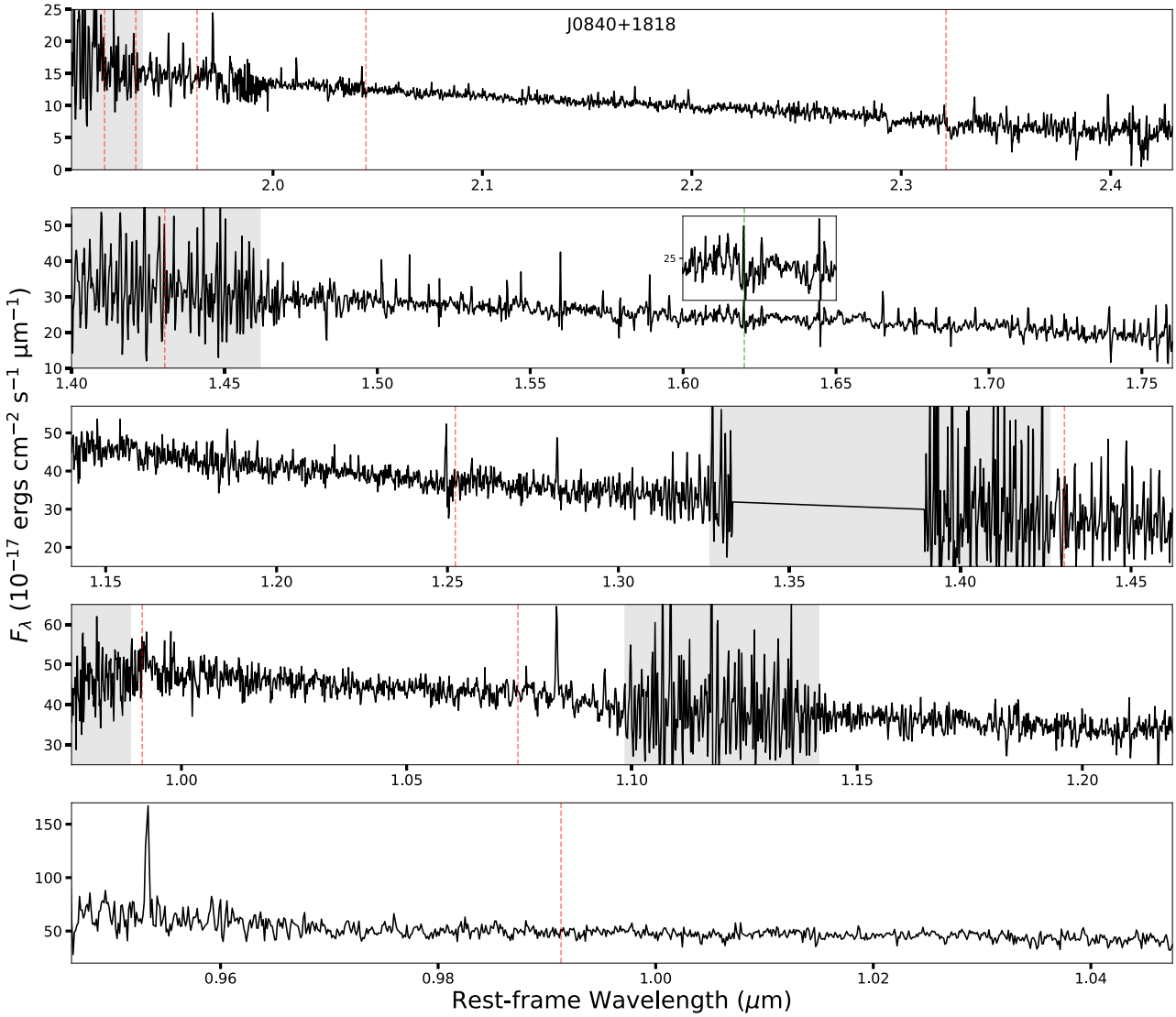

Figure 8. Same as Figure 7 but for J0840+1818.

Table 7
J0840 Emission Line Parameters

Emission	FWHM (km s^{-1})	Flux (10^{-17} erg cm^{-2} s^{-1})	Notes
[S III] 0.9531 μm	82 ± 2	410 ± 4	Low transmission
He I 1.0830 μm	89 ± 4	109 ± 2	…
Paγ 1.0941 μm	10^{+19}_{-10}	32 ± 2	Within telluric absorption
[Fe II] 1.2567 μm	43 ± 31	28 ± 4	On skyline
Paβ 1.2822 μm	3^{+34}_{-3}	57 ± 4	On skyline
Brγ 2.1661 μm	152 ± 140	11 ± 5	…
CO(6-3) 1.62 μm	518 ± 126	…	Absorption feature, on skyline

Note. Same as Table 6. The depth of the absorption feature measures about 14% of the continuum, suggesting roughly 70% of the H-band continuum comes from GMK red giants.

components) and velocity offsets (up to -60 km s^{-1}) indicate that the outflow could be traced by this single profile.

The NIR spectrum of J0811+2328 is shown in Figure 7 and line measurements are listed in Table 6. We detect no NIR CL emission at the 2σ level, though deeper observations could reveal faint [S VIII], [Fe XIII], [S IX], and [Ca VIII]. These lines either fall on skylines or their S/N is consistent with the noise level so we do not include them in our analysis. The rest of the spectrum is relatively featureless aside from a handful of typically strong NIR lines, such as [S III] 0.9531 μm and He I 1.0830 μm. Unfortunately, the CN absorption at 1.1 μm falls within heavy telluric absorption so we cannot make an estimate on the contribution of a younger stellar population.

A.3. J084025.54+181858.99

Like J0811+2328, Moran et al. (2014) also reported a lower limit to the black hole (BH) mass for J0840+1818, $\log(M_{\rm BH}/M_\odot) > 4.3$. MC20 reported evidence of disturbed

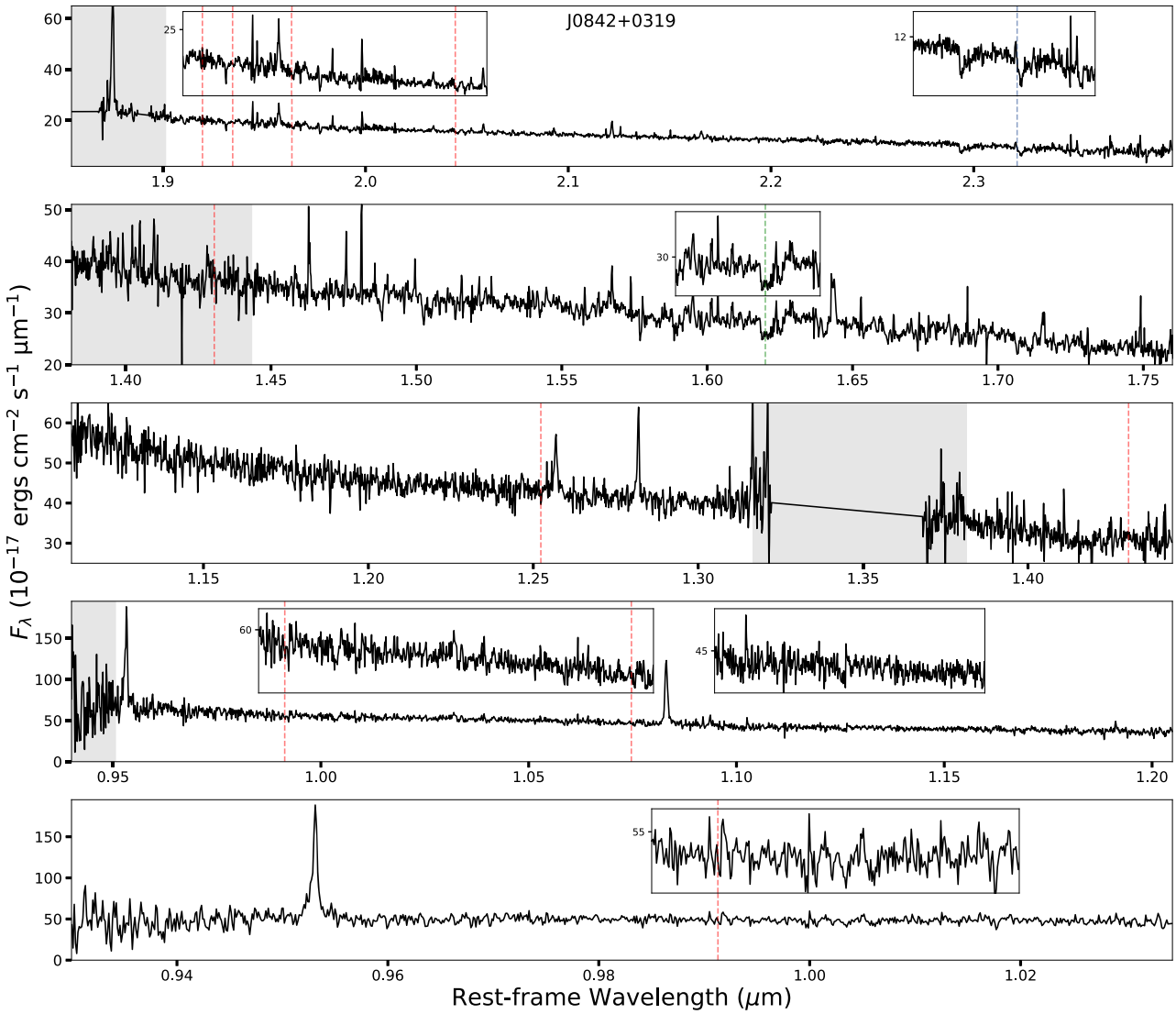

Figure 9. Same as Figure 7 but for J0842+1818. The blue-dashed line indicates a CL with a 2σ detection.

gas and MK19 detect an outflow through a multicomponent fit to [O III]. Data from L20, however, show velocity offsets ranging from -30 km s^{-1} to $+20$ km s^{-1} and only a single Gaussian was used in the fit. In addition, the line widths are smaller than the velocity dispersions of the stellar component. This all suggests that the gas is rotating in the same direction as the stars and they found no clear evidence of outflows in their data.

The NIR spectrum of J0840+1818 is shown in Figure 8 and line measurements are listed in Table 7. We find no CLs at the 2σ detection level, though faint [Ca VIII] may be present. Similar to J0811+2328, we only detect a handful of emission lines and the 1.1 μm CN absorption falls within significant telluric absorption. MK19 do report the optical CL [Ne V] λ3426 emission.

A.4. J084234.50+031930.68

MK19 reported broad Hα J0842+0319, from which they calculated a BH mass of $\log(M_{\rm BH}/M_\odot) = 5.84$. MC20 reported both disturbed and stratified gas, which is consistent with the findings of L20 where they found blueshifted gas up to -160 km s^{-1}.

The NIR spectrum of J0842+0319 is shown in Figure 9 and line measurements are listed in Table 8. We detect [Ca VIII] as the only NIR CL in this object. To provide a more accurate measurement of the flux and width, we include simultaneous fits to the CO band absorption. Of the objects that show NIR CL emission, J0842+0319 has the lowest $L_{\rm AGN}$ and deepest CO(6-3) band absorption feature. Deeper observations may reveal other, more faint CLs. The rest of the spectrum shows a number of hydrogen recombination, H_2, and He I lines, and significant CN absorption is seen, suggesting an older stellar population.

A.5. J090613.75+561015.5

Reines & Volonteri (2015) reported a BH mass of $\log(M_{\rm BH}/M_\odot) = 5.40$, based on virial mass estimates. Marleau et al. (2017) also reported a BH mass using bolometric luminosities from WISE IR data, from which they calculate $\log(M_{\rm BH}/M_\odot) = 6.93$. Baldassare et al. (2017) reported bright X-ray emission, $L_{0.5-7\ \rm keV} = 4.47 \times 10^{40}$ erg s^{-1}, in Chandra data that is higher than what is expected from high-mass X-ray binaries. They concluded that AGN activity is the likely source of this X-ray emission. MC20 reported disturbed gas and three

Table 8
J0842 Emission Line Parameters

Emission	FWHM (km s^{-1})	Flux (10^{-17} erg cm^{-2} s^{-1})	Notes
[S III] 0.9531 μm total	⋯	950 ± 14	Order 7, $F > 2$
Narrow	62 ± 3	341 ± 8	Order 7
Broad	415 ± 8	609 ± 11	Order 7
[S III] 0.9531 μm total	⋯	986 ± 19	Order 6, low transmission, $F = 2$
Narrow	62 ± 6	310 ± 12	Order 6
Broad	350 ± 6	677 ± 15	Order 6
Paϵ 0.9549 μm	155 ± 16	76 ± 5	Order 7, blend with [S III]λ 9531
Paϵ 0.9549 μm	171 ± 15	103 ± 6	Order 6, blend with [S III]λ 9531
Paδ 1.0052 μm	48 ± 34	24 ± 3	Order 7
Paδ 1.0052 μm	77 ± 60	24 ± 4	Order 6
[S II] 1.0323 μm	299 ± 40	71 ± 7	…
[S II] 1.0339 μm	71 ± 40	20 ± 4	…
He I 1.0830 μm	200 ± 6	618 ± 13	…
[Fe II] 1.2567 μm	280 ± 46	159 ± 16	…
Paβ 1.2822 μm	127 ± 12	152 ± 28	Blue asymmetric tail
[Fe II] 1.6435 μm	269 ± 27	152 ± 12	On skyline
Paα 1.8756 μm	192 ± 3	661 ± 7	Within telluric absorption
H_2 1.9576 μm	165 ± 21	84 ± 7	…
H_2 2.0338 μm	129 ± 74	17 ± 5	On skyline
He I 2.0587 μm	64 ± 34	25 ± 4	On skyline
H_2 2.1218 μm	82 ± 13	53 ± 3	…
Brγ 2.1661 μm	136 ± 29	30 ± 4	…
H_2 2.2235 μm	50 ± 35	14 ± 5	…
[Ca VIII] 2.3214 μm	90 ± 53	29 ± 13	…
CO(6-3) 1.62 μm	723 ± 136	⋯	Absorption feature

Note. Same as Table 6. The depth of the absorption feature measures about 13% of the continuum, suggesting roughly 65% of the *H*-band continuum comes from GMK red giants.

components were used in the fits done by L20. Maximum widths of the third component reach up 1250 km s^{-1}, the largest seen in the sample and is indicative of a fast outflow.

We also note that the C2 component of [O III] measured in L20 is redshifted 60 km s^{-1} relative to the systemic velocity. One explanation for this is that they are observing the far side of the outflow. Interestingly, this redshifted component is also seen in [Si VI], where it is offset by ∼90 km s^{-1}. Since the two values are consistent with each other, we are both likely observing the far side of the outflow.

The NIR spectrum of J0906+5610 is shown in Figure 10 and line measurements are listed in Table 9. The spectrum has an abundant number of emission lines, including strong hydrogen recombination, H_2, and He I lines. The CL emission is also strong, with significant emission from [Si VI], [S IX], and [Si X]. We also detect weaker emission from [S VIII] and [Ca VIII]. [Si VI] is best fit with two Gaussian components (see Figure 11), while only one Gaussian was necessary to fit the other CLs properly. It is noteworthy that [Si VI] falls within a region of telluric absorption and skylines. However, on closer inspection of the telluric standard star used, the degree of absorption is comparable to that seen redward at 1.98 μm. Thus, we expect the noise level around [Si VI] to be at similar levels. The skylines are also similar to those blueward and the effects can be seen in the residuals of the fit. Lastly, we do not detect CN absorption in the *J* band.

Inspection of the available optical data from SDSS, LRIS, GMOS, and KCWI yields a number of CLs. These include [Ne V] λ3426, [Fe VII] $\lambda\lambda\lambda$5721, 5159, 6087, and [Fe X] λ6374.

A.6. J095418.16+471725.1

Both Reines & Volonteri (2015) and Marleau et al. (2017) reported a BH mass for J0954+4717. Using the methods described in Section A.5, they reported $\log(M_{\rm BH}/M_\odot)$ equal to 5.00 and 6.46, respectively. Similar to J0906+5610, Baldassare et al. (2017) also reported strong X-ray emission, $L_{0.5\text{–}7\ \rm keV} = 9.77 \times 10^{39}$ erg s^{-1} that is likely coming from AGN activity. MC20 reported disturbed gas, and as shown in L20, three components were needed to properly describe the profile. Both of these indicate the presence of outflows.

The NIR spectrum of J0954+4717 is shown in Figure 12 and line measurements are listed in Table 10. Strong emission is seen in various hydrogen recombination, H_2, and He I lines. A large number of these emission lines require a multi-component fit to properly match their profile, possibly due to the outflow. [Si VI], plotted in Figure 13, is the only strong CL. Inspecting the skyline immediately on top of [Si VI], we find it to be of similar strength to those redward. As shown in the bottom panel, the residuals at the locations of the skylines are comparable, leading us to believe our fit is representative of the emission. Evaluating the emission profile of [Si VI], we obtain an *F*-test value of ∼1.5 when adding a broad component. Although this is suggestive of the presence of broad emission, we cannot say for certain whether adding a broad component is justifiable. As such, we treat this as an upper limit to the broad flux and width.

In addition to [Si VI], we also detect two sulfur lines, [S VIII] and [S IX]. Similar to the other galaxies in our sample, we do not detect any CN absorption in the *J* band.

Like J0906+5610, inspection of the available optical data from SDSS, LRIS, GMOS, and KCWI yields a number of CLs. These include [Ne V] $\lambda\lambda$ 3346, 3426, [Fe V] λ3839, and [Fe VII] $\lambda\lambda$ 5159, 6087.

A.7. J100551.19+125740.6

Marleau et al. (2017) reported a BH mass of $\log(M_{\rm BH}/M_\odot) = 6.47$ and MC20 found disturbed gas in their optical data. Like J0811+2328, Wang et al. (2016) reported a $L_{0.3\text{–}8\ \rm keV}$ flux for J1005+1257, from which we obtain a $L_{2\text{–}10\ \rm keV}$ of 5.20×10^{39} erg s^{-1}. L20 fit three components to the [O III] emission line profile, and the broadest component, C3, have widths up to 1200 km s^{-1}. This is the second broadest they see in the sample and suggests the presence of a fast outflow.

The NIR spectrum of J1005+1257 is shown in Figure 14 and line measurements are listed in Table 11. Like the other galaxies with CL emission, its spectrum shows a wealth of strong emission lines. Of particular note is [Si VI], which shows a strong broad component (see Figure 15, right). Unfortunately, the emission falls in a number of small telluric absorption features, but they do not drastically alter the fit. The region that was most affected was the large telluric feature redward of the [Si VI] line. In order to not overestimate the [Si VI] emission,

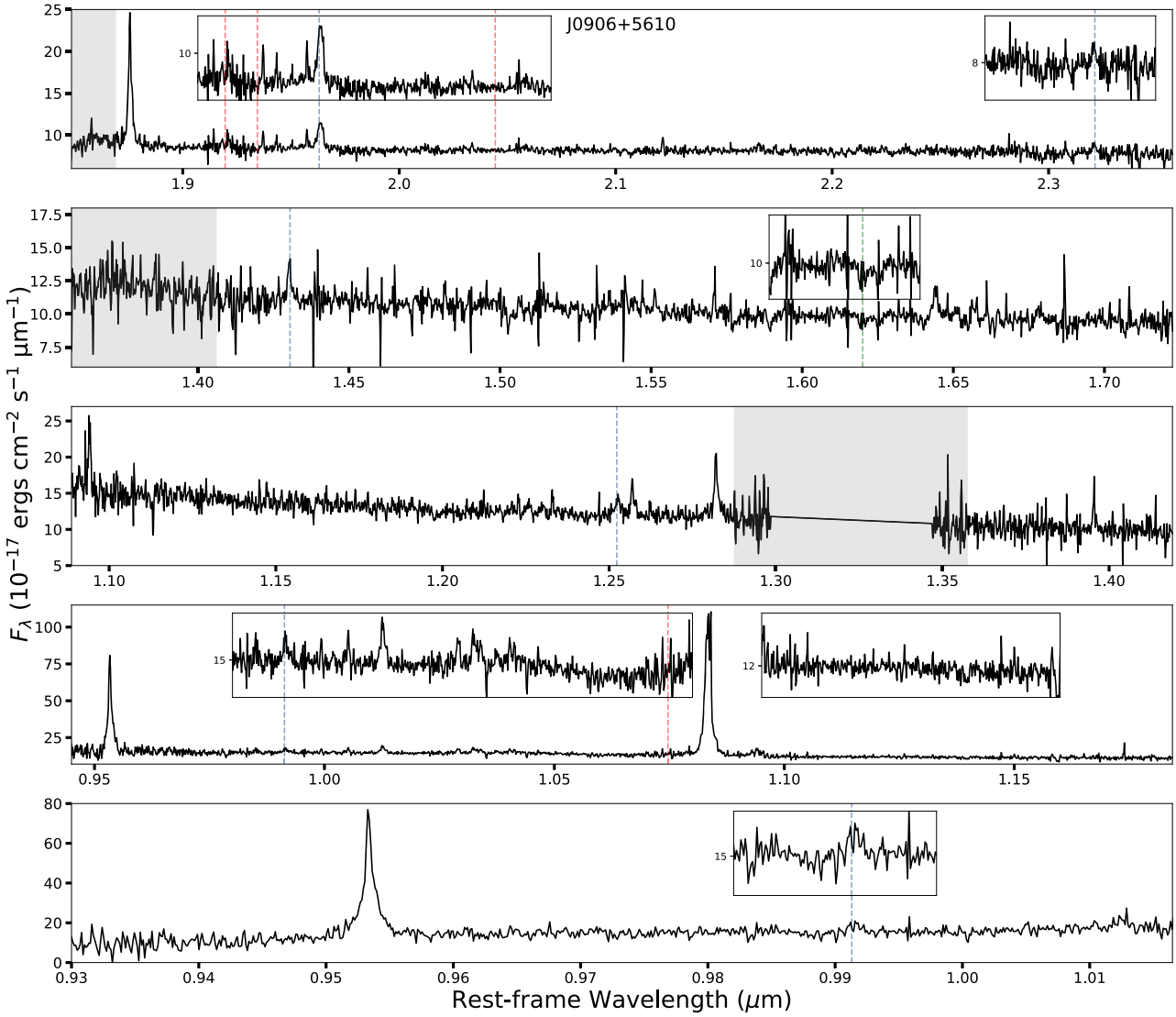

Figure 10. Same as Figure 7 but for J0906+5610.

particularly the broad component, we masked out the entire telluric feature (as represented as the large yellow block) from the fit.

We also detect strong emission of [Si X] and [S IX], and weaker emission of [S VIII] and [Ca VIII]. We detect [Si X] in two NIRES orders and list both measurements. We select the values from order 5 since the S/N is higher and the measurements are less uncertain. Also, we do not detect any CN absorption in the *J* band.

Optical data reveal [Fe X] λ6374 emission and possible [Fe VII] λ5721 emission. The relative abundance of NIR CL emission and lack of optical CL emission is not surprising since J1005+1257 exhibits the highest extinction of our sample (see Table 2).

A.8. J100935.66+265648.9

Moran et al. (2014) provided an upper limit to the BH mass through Eddington luminosity arguments, $\log(M_{\rm BH}/M_\odot) > 5.1$. In addition, MC20 reported disturbed gas and a two-component fit was needed to properly fit the IFU data in L20. Due to the kinematic differences and velocity offsets between the C1 and C2 components, they suggested that the C2 component could represent a tilted, biconcial outflow, similar to that of J0100-0110.

The NIR spectrum of J1009+2656 is shown in Figure 16 and line measurements are listed in Table 12. Only one component is needed to properly fit [Si VI] (see Figure 17), this being the only case in our sample. Although there appears to be a red broad component, closer inspection of the standard star reveals telluric absorption in that region, which leads us to believe that it is due to a poorly corrected telluric feature. We also detect weak emission in [S VIII], [S IX], and [Ca VIII]. Lastly, we detect no CN absorption.

We also detect the optical CL [Ne V] λ3426, with other possible detections including [Fe VII] $\lambda\lambda$ 5721, 6087. Deeper observations will be needed to confirm these detections.

A.9. J144252.78+205451.67

J1442+2054 is one of two galaxies in our sample that falls in the composite region of the BPT diagram (see MK19). MC20 found both disturbed and stratified gas in

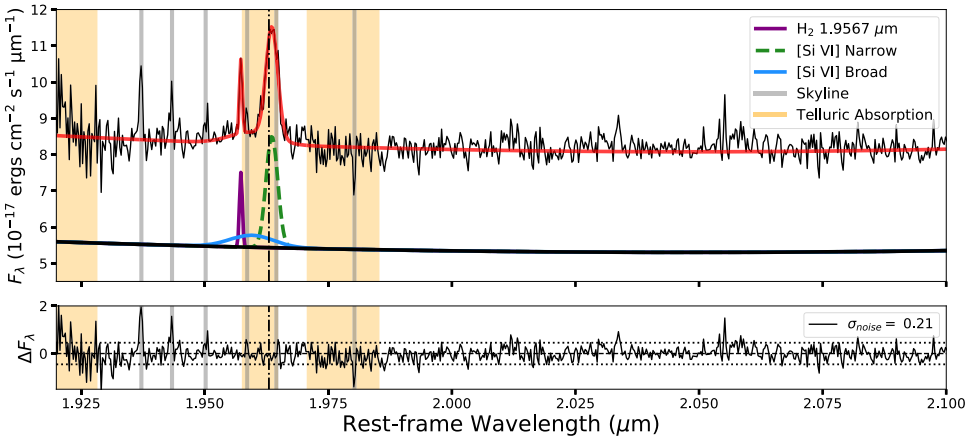

Figure 11. MCMC fit to [Si VI]1.9630 μm and $H_2$1.9576 μm emission for J0906. The spectrum is shifted to rest-frame wavelength using the systemic redshift. The purple line represents the fit to the H_2 emission, while the green-dotted and blue line fits represent the narrow and broad components of [Si VI]. The bottom panels show residuals to the fits and 1σ noise level (represented as dotted lines). The location of skylines and regions of telluric absorption near [Si VI] are represented as gray and and yellow lines, respectively. Note that running an *F*-test on these fits suggests that a two-component fit is needed.

Table 9
J0906 Emission Line Parameters

Emission	FWHM (km s^{-1})	Flux (10^{-17} erg cm^{-2} s^{-1})	Notes
[S III] 0.9531 μm total	⋯	710 ± 6	Order 7, $F > 2$
Narrow	104 ± 3	168 ± 4	Order 7
Broad	657 ± 9	542 ± 5	Order 7
[S III] 0.9531 μm total	⋯	694 ± 16	Order 6, low transmission, $F > 2$
Narrow	88 ± 8	163 ± 10	Order 6
Broad	630 ± 25	531 ± 12	Order 6
[S VIII] 0.9913 μm	277 ± 20	32 ± 2	Order 7, on skyline
[S VIII] 0.9913 μm	381 ± 77	29 ± 9	Order 6, on skyline
Paδ 1.0052 μm	92 ± 29	15 ± 2	Order 6
He II 1.0126 μm	306 ± 73	42 ± 8	…
[S II] 1.0289 μm	206 ± 71	21 ± 5	On skyline
[S II] 1.0323 μm	350 ± 122	35 ± 9	Blend with [S II] 1.0339 μm
[S II] 1.0339 μm	235.16 ± 127.78	16 ± 8	Blend with [S II] 1.0323 μm
[N I] 1.0400 μm	151 ± 77	15 ± 5	…
He I 1.0830 μm total	⋯	1660 ± 45	On skyline, within telluric absorption, $F > 2$
Narrow	394 ± 5	1260 ± 33	…
Broad	1081 ± 81	401 ± 31	…
[S IX] 1.2523 μm	299 ± 53	31 ± 4	…
[Fe II] 1.2567 μm	199 ± 23	44 ± 3	On skyline
Paβ 1.2822 μm	282 ± 27	102 ± 6	On skyline
[Si X] 1.4305 μm	309 ± 58	46 ± 6	…
[Fe II] 1.6435 μm	344 ± 57	44 ± 5	On skyline
Paα 1.8756 μm total	⋯	300 ± 19	On skyline, $F > 2$
Narrow	71 ± 30	66 ± 13	…
Broad	440 ± 37	234 ± 14	…
H_2 1.9576 μm	63 ± 36	15 ± 2	On skyline
[Si VI] 1.9630 μm total	⋯	127 ± 15	On skyline, within telluric absorption, $F > 2$
Narrow	424 ± 29	92 ± 7	…
Broad	1683 ± 479	35 ± 13	…
H_2 2.0338 μm	97 ± 44	7 ± 1	…
H_2 2.1218 μm	81 ± 42	14 ± 3	…
Brγ 2.1661 μm	174 ± 34	13 ± 3	…
[Ca VIII] 2.3214 μm	397 ± 131	33 ± 8	…
CO(6-3) 1.62 μm	508 ± 135	⋯	Absorption feature, on skyline

Note. Same as Table 6. The depth of the absorption feature measures about 10% of the continuum, suggesting roughly 50% of the *H*-band continuum comes from GMK red giants.

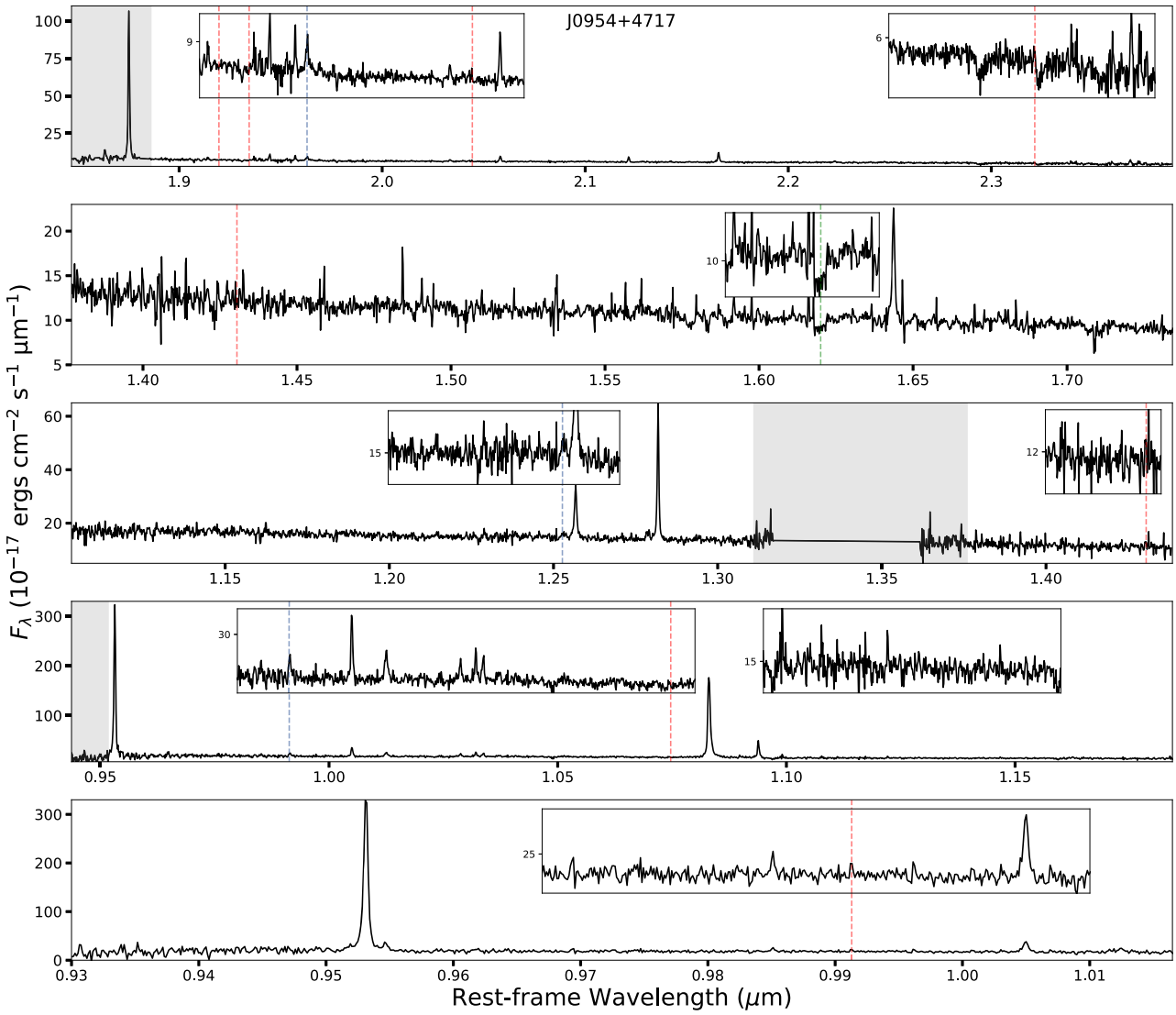

Figure 12. Same as Figure 7 but for J0954+4717.

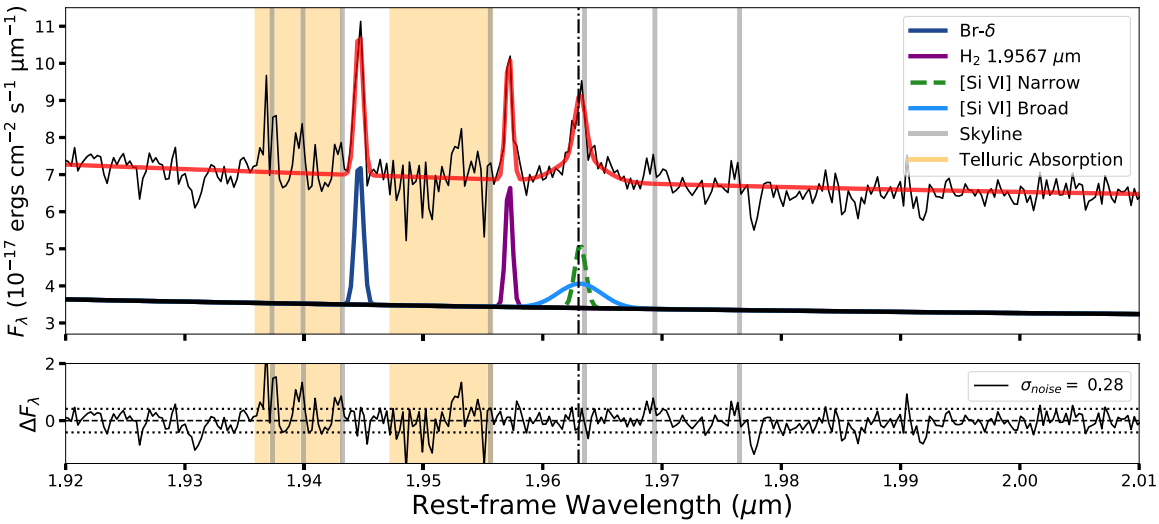

Figure 13. Same as Figure 11 but for J0954+4717. We additionally fit Brδ, represented as a cobalt-colored line.

Table 10
J0954 Emission Line Parameters

Emission	FWHM (km s^{-1})	Flux (10^{-17} erg cm^{-2} s^{-1})	Notes
[S III] 0.9531 μm total	⋯	1719 ± 75	Order 7, $F > 2$
Narrow	87 ± 2	1251 ± 56	Order 7
Broad	530 ± 36	468 ± 46	Order 7
[S III] 0.9531 μm total	⋯	1736 ± 74	Order 6, $F > 2$
Narrow	73 ± 2	1147 ± 60	Order 6
Broad	401 ± 21	590 ± 43	Order 6
Paϵ 0.9549 μm	75 ± 24	52 ± 10	Order 7, blend with [S III]λ 9531
Paϵ 0.9549 μm	129 ± 42	64 ± 13	Order 6
[C I] 0.9853 μm	75 ± 45	24 ± 8	Order 7, on skyline
[S VIII] 0.9913 μm	109 ± 30	30 ± 5	Order 6
Paδ 1.0052 μm	119 ± 10	108 ± 8	Order 7, on skyline
Paδ 1.0052 μm	102 ± 12	89 ± 8	Order 6, on skyline
He II 1.0126 μm	194 ± 23	56 ± 6	…
[S II] 1.0289 μm	128 ± 44	28 ± 7	…
[S II] 1.0323 μm	80 ± 28	38 ± 7	…
[S II] 1.0339 μm	128 ± 29	37 ± 7	…
He I 1.0830 μm total	⋯	1391 ± 44	Red asymmetric tail, $F > 2$
Narrow	152 ± 5	1065 ± 35	…
Broad	805 ± 61	325 ± 26	…
Paγ 1.0941 μm	96 ± 7	162 ± 10	On skyline
[S IX] 1.2523 μm	387 ± 116	24 ± 9	On skyline
Fe II 1.2567 μm total	⋯	197 ± 57	On skyline, $F = 2$
Narrow	125 ± 19	102 ± 39	…
Broad	400 ± 124	95 ± 42	…
Paβ 1.2822 μm total	⋯	342 ± 53	On skyline, $F > 2$
Narrow	59 ± 18	186 ± 40	…
Broad	252 ± 64	157 ± 35	…
Fe II 1.6435 μm total	⋯	150 ± 21	On skyline, $F > 2$
Narrow	114 ± 16	90 ± 15	…
Broad	440 ± 115	61 ± 15	…
Paα 1.8756 μm total	⋯	952 ± 36	Within telluric absorption, $F > 2$
Narrow	63 ± 5	655 ± 27	…
Broad	309 ± 30	298 ± 24	…
Brδ 1.9451 μm	83 ± 11	33 ± 2	Within telluric absorption
H_2 1.9576 μm	64 ± 28	25 ± 3	…
[Si VI] 1.9630 μm total	⋯	53 ± 11	On skyline, $F \sim 1.5$
Narrow	142 ± 54	19 ± 7	…
Broad	687 ± 164	35 ± 8	…
H_2 2.0338 μm	117 ± 29	11 ± 2	…
He I 2.0587 μm	111 ± 8	35 ± 2	…
H_2 2.0735 μm	105 ± 60	4 ± 2	…
H_2 2.1218 μm	71 ± 12	28 ± 2	…
Brγ 2.1661 μm total	⋯	79 ± 10	$F > 2$
Narrow	60 ± 19	45 ± 7	…
Broad	374 ± 94	35 ± 7	…
H_2 2.2235 μm	160 ± 39	12 ± 2	…
CO(6-3) 1.62 μm	553 ± 63	⋯	Absorption feature

Note. Same as Table 6. The depth of the absorption feature measures about 11% of the continuum, suggesting roughly 55% of the *H*-band continuum comes from GMK red giants.

their optical data. This object was not observed in L20 and no BH mass has been reported to date.

The NIR spectrum of J1442+2054 is shown in Figure 18 and line measurements are listed in Table 13. The NIR is relatively featureless, with only a handful of typically strong emission lines appearing. We detect no CL emission (optical nor NIR) in this galaxy. We also do not detect any CN absorption.

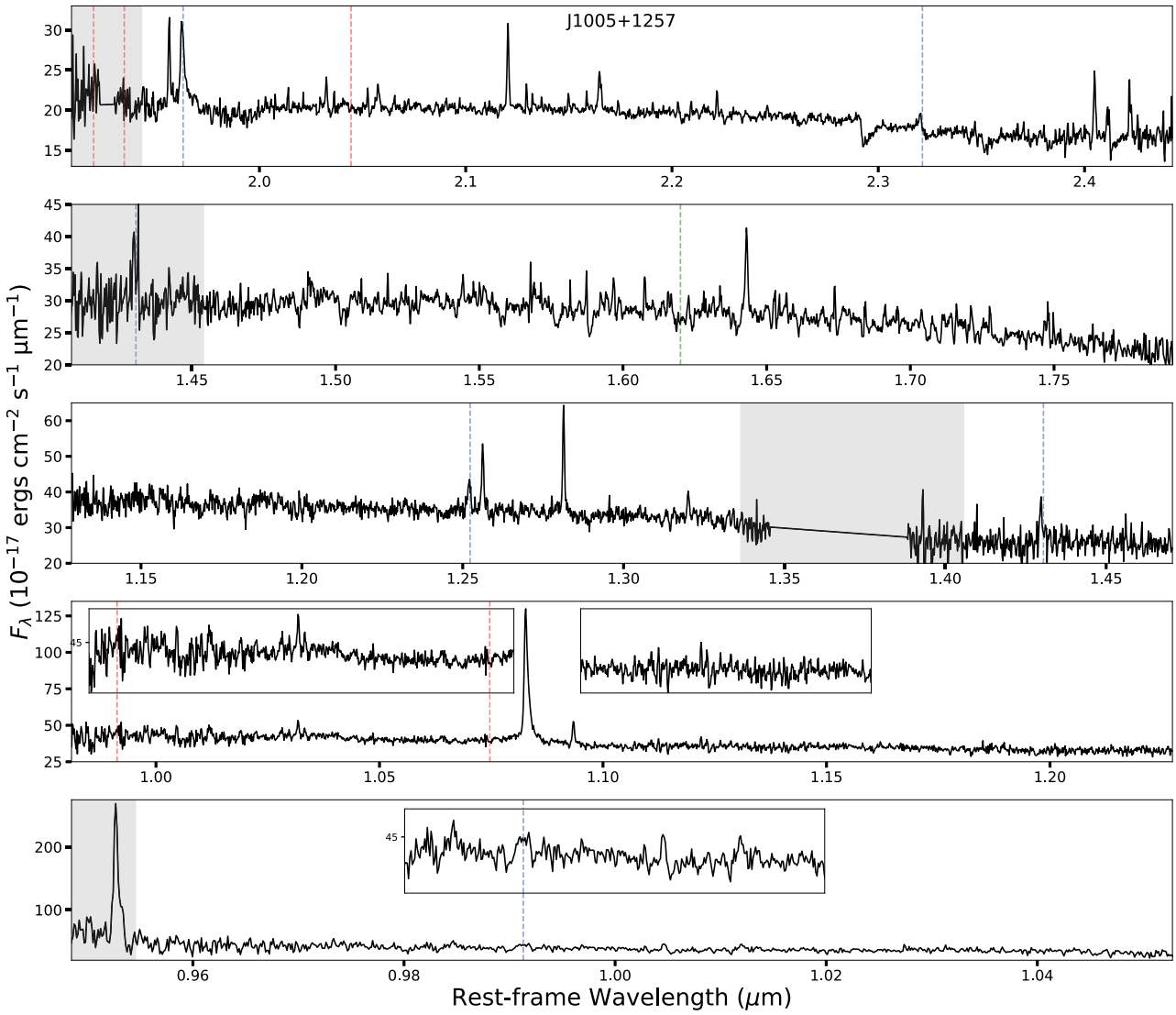

Figure 14. Same as Figure 7 but for J1005+1257.

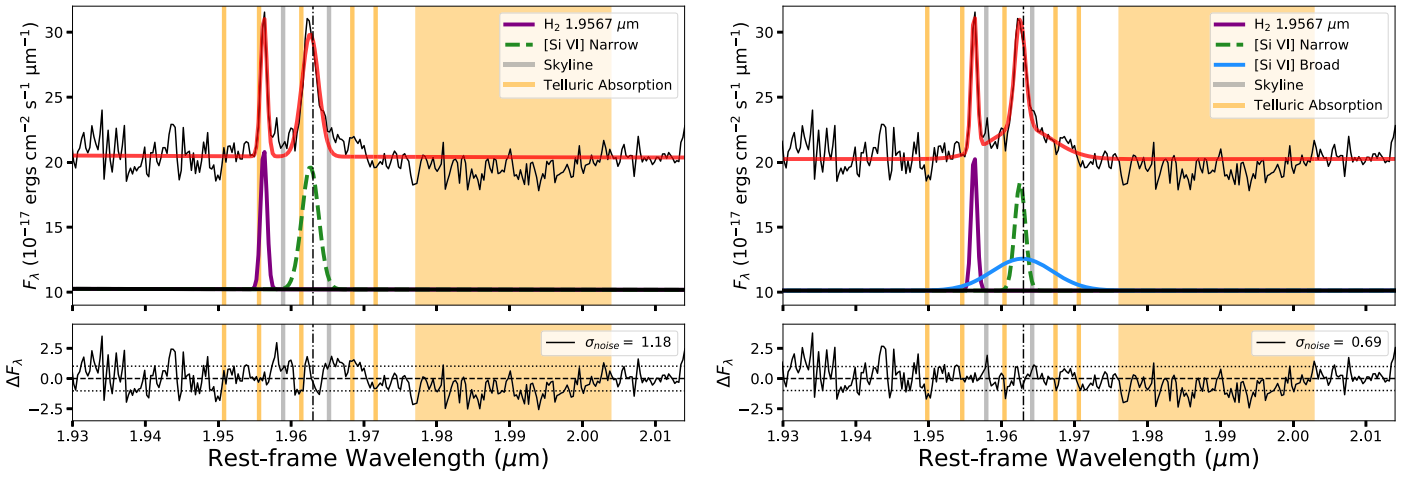

(a) (b)

Figure 15. Same as Figure 11 but for J1005+1257. We plot a single-component fit (left) and a double-component fit (right). Note that running an F-test on these fits suggests that a two-component fit is needed.

Table 11
J1005 Emission Line Parameters

Emission	FWHM (km s^{-1})	Flux (10^{-17} erg cm^{-2} s^{-1})	Notes
[S III] 0.9531 μm	144 ± 4	2504 ± 220	Low transmission, red asymmetric tail
[C I] 0.9853 μm	215 ± 18	134 ± 15	…
[S VIII] 0.9913 μm	299 ± 9	142 ± 14	On skyline
Paδ 1.0052 μm	77 ± 5	74 ± 8	Order 7
He II 1.0126 μm	173 ± 53	105 ± 30	Order 7
He II 1.0126 μm	202 ± 36	102 ± 22	Order 6
[S II] 1.0289 μm	185 ± 45	66 ± 15	…
[S II] 1.0323 μm	145 ± 20	134 ± 19	On skyline
[S II] 1.0339 μm	109 ± 36	59 ± 13	…
He I 1.0830 μm total	…	2433 ± 194	On skyline, $F > 2$
Narrow	243 ± 5	1458 ± 96	…
Broad	1337 ± 89	976 ± 117	…
Paγ 1.0941 μm	130 ± 11	179 ± 19	…
[S IX] 1.2523 μm	256 ± 38	160 ± 25	…
[Fe II] 1.2567 μm	169 ± 17	251 ± 26	On skyline
Paβ 1.2822 μm	133 ± 9	348 ± 28	…
[Fe II] 1.3208 μm	143 ± 6	92 ± 6	On skyline
[Si X] 1.4305 μm	162 ± 4	164 ± 8	Order 5, within telluric absorption
[Si X] 1.4305 μm	156 ± 18	168 ± 20	Order 4, within telluric absorption
[Fe II] 1.6435 μm	157 ± 17	188 ± 17	…
H_2 1.9576 μm	114 ± 11	135 ± 11	Within telluric absorption
[Si VI] 1.9630 μm total	…	491 ± 31	On skyline, within telluric absorption, $F > 2$
Narrow	246 ± 14	193 ± 16	…
Broad	1376 ± 114	298 ± 27	…
H_2 2.0338 μm	106 ± 35	43 ± 8	…
He I 2.0587 μm	202 ± 56	47 ± 10	…
H_2 2.1218 μm	121 ± 7	137 ± 7	…
Brγ 2.1661 μm	208 ± 19	95 ± 8	On skyline
H_2 2.2235 μm	55 ± 35	28 ± 6	…
[Ca VIII] 2.3214 μm	291 ± 129	48 ± 18	…
H_2 2.4066 μm	104 ± 18	104 ± 12	…
CO(6-3) 1.62 μm	778 ± 232	…	Absorption feature

Note. Same as Table 6. The depth of the absorption feature measures about 7% of the continuum, suggesting roughly 35% of the *H*-band continuum comes from GMK red giants.

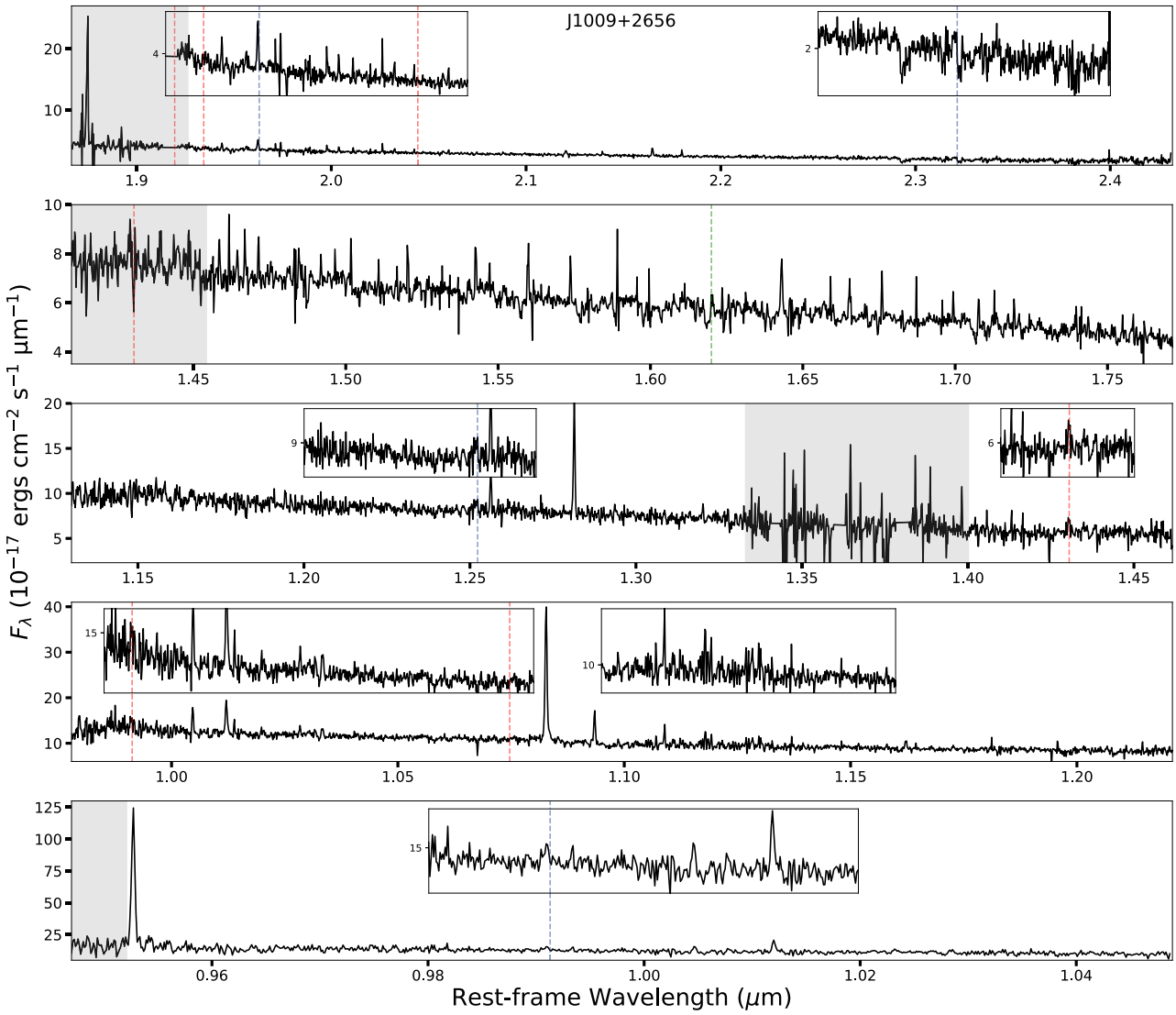

Figure 16. Same as Figure 7 but for J1009+2656.

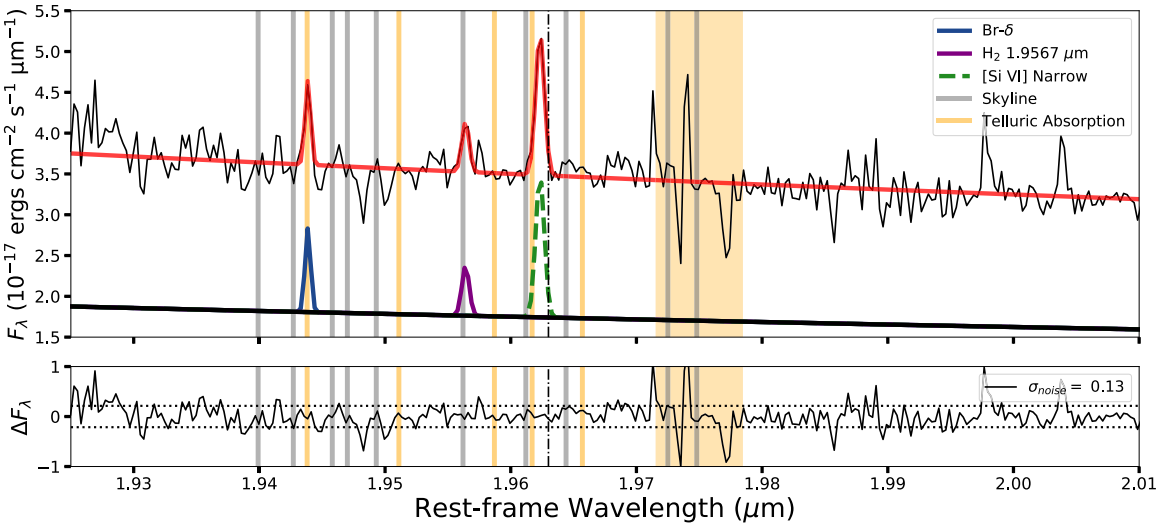

Figure 17. Same as Figure 13 but for J1009+2656. No broad component could be fit.

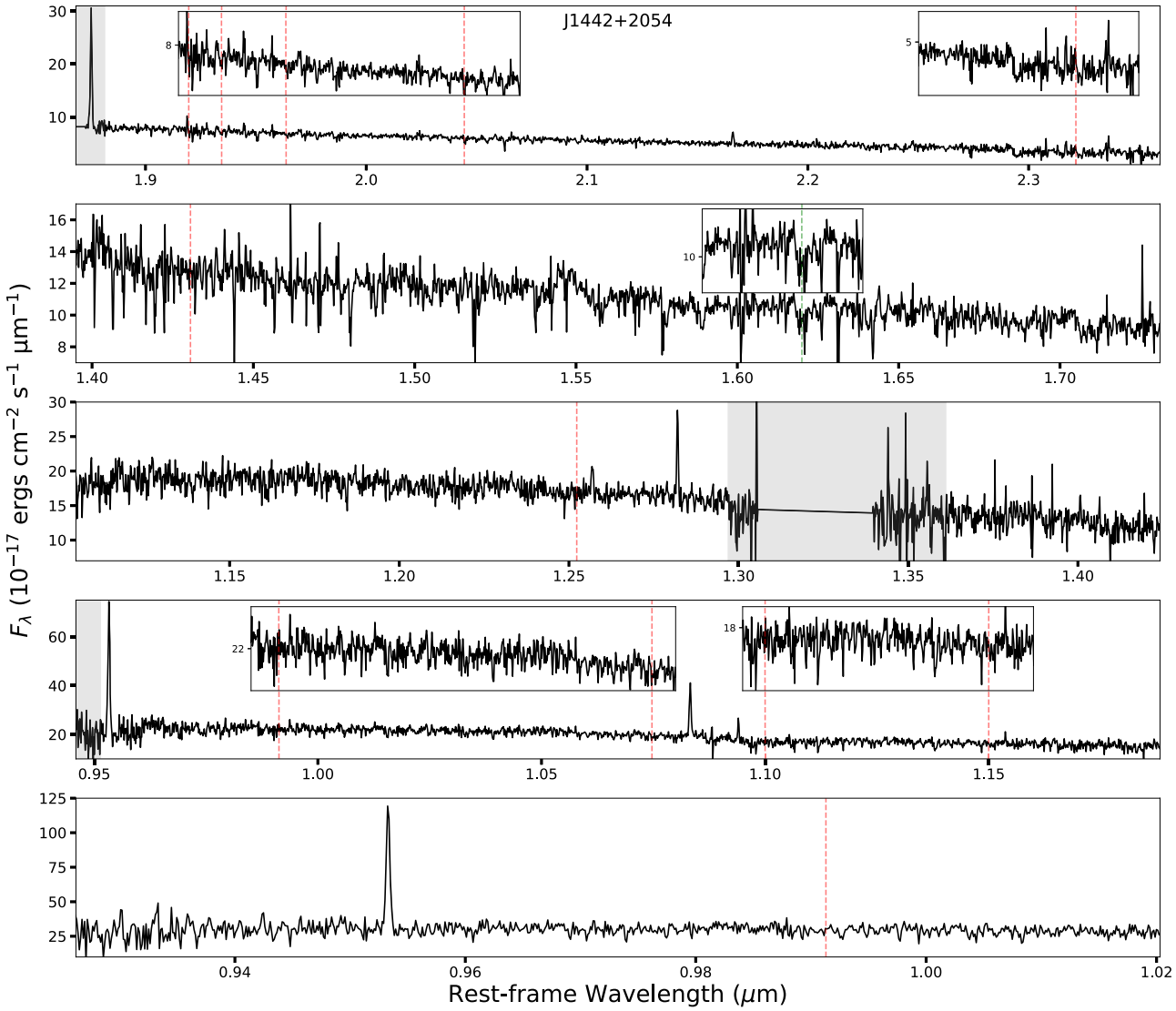

Figure 18. Same as Figure 7 but for J1442+2054.

Table 12
J1009 Emission Line Parameters

Emission	FWHM (km s^{-1})	Flux (10^{-17} erg cm^{-2} s^{-1})	Notes
[S III] 0.9531 μm	83 ± 1	507 ± 20	Order 7
[S III] 0.9531 μm	128 ± 2	552 ± 26	Order 6, low transmission
Paϵ 0.9549 μm	125 ± 7	47 ± 4	Order 7
[S VIII] 0.9913 μm	145 ± 40	17 ± 4	Order 7
Paδ 1.0052 μm	44 ± 17	14 ± 2	Order 7
Paδ 1.0052 μm	26 ± 21	23 ± 3	Order 6
He II 1.0126 μm	67 ± 22	39 ± 6	Order 7
He II 1.0126 μm	114 ± 13	44 ± 4	Order 6
[S II] 1.0339 μm	92 ± 37	9 ± 3	…
He I 1.0830 μm	116 ± 3	189 ± 8	Red asymmetric tail, $F < 2$
Paγ 1.0941 μm	71 ± 30	35 ± 7	…
He I 1.1629 μm	106 ± 45	22 ± 3	…
[S IX] 1.2523 μm	269 ± 90	11 ± 3	On skyline
[Fe II] 1.2567 μm	71 ± 16	22 ± 2	On skyline
Paβ 1.2822 μm	83 ± 6	68 ± 2	…
[Fe II] 1.6435 μm	83 ± 22	18 ± 2	…
Paα 1.8756 μm	86 ± 2	197 ± 7	Within telluric absorption

Table 12
(Continued)

Emission	FWHM (km s^{-1})	Flux (10^{-17} erg cm^{-2} s^{-1})	Notes
Brδ 1.9451 μm	INDEF	6 ± 1	Within telluric absorption, width < telescope spectral resolution
H_2 1.9576 μm	76 ± 34	5 ± 1	On skyline
[Si VI] 1.9630 μm	99 ± 15	17 ± 1	Adjacent to skyline
H_2 2.0338 μm	48^{+26}_{-48}	5 ± 1	…
He I 2.0587 μm	117 ± 70	4 ± 1	…
H_2 2.1218 μm	128 ± 26	8 ± 1	On skyline
Brγ 2.1661 μm	63 ± 22	12 ± 1	…
[Ca VIII] 2.3214 μm	323 ± 79	12 ± 6	…
CO(6-3) 1.62 μm	237 ± 39	…	Absorption feature

Note. Same as Table 6. The depth of the absorption feature measures about 11% of the continuum, suggesting roughly 55% of the *H*-band continuum comes from GMK red giants.

Table 13
J1442 Emission Line Parameters

Emission	FWHM (km s^{-1})	Flux (10^{-17} erg cm^{-2} s^{-1})	Notes
[S III] 0.9531 μm	88 ± 2	435 ± 29	Order 7
[S III] 0.9531 μm	115 ± 2	315 ± 20	Order 6, low transmission
He I 1.0830 μm	115 ± 9	138 ± 12	In telluric absorption
Paγ 1.0941 μm	24 ± 2	36 ± 6	In telluric absorption
[Fe II] 1.2567 μm	134 ± 51	33 ± 8	…
Paβ 1.2822 μm	86 ± 15	83 ± 9	…
[Fe II] 1.6435 μm	137 ± 65	17 ± 5	…
Paα 1.8756 μm	93 ± 4	203 ± 7	On skyline, in telluric absorption
He I 2.0587 μm	103 ± 60	8 ± 2	…
Brγ 2.1661 μm	75 ± 26	21 ± 3	…
H_2 2.2477 μm	115 ± 43	12 ± 2	…
CO(6-3) 1.62 μm	446 ± 133	…	Absorption feature, on skyline

Note. Same as Table 6. The depth of the absorption feature measures about 11% of the continuum, suggesting roughly 55% of the *H*-band continuum comes from GMK red giants.

ORCID iDs

Thomas Bohn https://orcid.org/0000-0002-4375-254X
Gabriela Canalizo https://orcid.org/0000-0003-4693-6157
Sylvain Veilleux https://orcid.org/0000-0002-3158-6820
Weizhe Liu https://orcid.org/0000-0003-3762-7344

References

Allen, M. G., Groves, B. A., Dopita, M. A., Sutherland, R. S., & Kewley, L. J. 2008, ApJS, 178, 20
Allington-Smith, J., Murray, G., Content, R., et al. 2002, PASP, 114, 892
Antonucci, R. 1993, ARA&A, 31, 473
Baldassare, V. F., Reines, A. E., Gallo, E., & Greene, J. E. 2017, ApJ, 836, 20
Baldwin, J. A., Phillips, M. M., & Terlevich, R. 1981, PASP, 93, 5
Becker, G. D., Rauch, M., & Sargent, W. L. W. 2009, ApJ, 698, 1010
Bradford, J. D., Geha, M. C., Greene, J. E., Reines, A. E., & Dickey, C. M. 2018, ApJ, 861, 50
Cann, J. M., Satyapal, S., Bohn, T., et al. 2020, ApJ, 895, 147
Cappellari, M., & Emsellem, E. 2004, PASP, 116, 138
Cardelli, J. A., Clayton, G. C., & Mathis, J. S. 1989, ApJ, 345, 245
Cerqueira-Campos, F. C., Rodríguez-Ardila, A., Riffell, R., et al. 2021, MNRAS, 500, 2666
Colina, L., Piqueras López, J., Arribas, S., et al. 2015, A&A, 578, A48
De Robertis, M. M., & Osterbrock, D. E. 1984, ApJ, 286, 171
De Robertis, M. M., & Osterbrock, D. E. 1986, ApJ, 301, 727
De Robertis, M. M., & Shaw, R. A. 1990, ApJ, 348, 421
Dong, R., Greene, J. E., & Ho, L. C. 2012, ApJ, 761, 73
Erkens, U., Appenzeller, I., & Wagner, S. 1997, A&A, 323, 707
Fabian, A. C. 2012, ARA&A, 50, 455
Ferguson, J. W., Korista, K. T., & Ferland, G. J. 1997, ApJS, 110, 287
Foreman-Mackey, D., Hogg, D. W., Lang, D., & Goodman, J. 2013, PASP, 125, 306
Gimeno, G., Roth, K., Chiboucas, K., et al. 2016, Proc. SPIE, 9908, 99082S
Groves, B. A., & Allen, M. G. 2010, NewA, 15, 614
Groves, B. A., Dopita, M. A., & Sutherland, R. S. 2004a, ApJS, 153, 9
Groves, B. A., Dopita, M. A., & Sutherland, R. S. 2004b, ApJS, 153, 75
Harrison, C. M., Alexander, D. M., Mullaney, J. R., & Swinbank, A. M. 2014, MNRAS, 441, 3306
Heckman, T. M., & Thompson, T. A. 2017, arXiv:1701.09062
Kelson, D. D. 2003, PASP, 115, 688
Kormendy, J., & Ho, L. C. 2013, ARA&A, 51, 511
Lamastra, A., Bianchi, S., Matt, G., et al. 2009, A&A, 504, 73
Lamperti, I., Koss, M., Trakhtenbrot, B., et al. 2017, MNRAS, 467, 540
Landt, H., Ward, M. J., Steenbrugge, K. C., & Ferland, G. J. 2015a, MNRAS, 449, 3795
Landt, H., Ward, M. J., Steenbrugge, K. C., & Ferland, G. J. 2015b, MNRAS, 454, 3688
Liu, W., Veilleux, S., Canalizo, G., et al. 2020, ApJ, 905, 166
Manzano King, C. 2020, PhD thesis, Univ. California, Riverside
Manzano-King, C. M., & Canalizo, G. 2020, MNRAS, 498, 4562
Manzano-King, C. M., Canalizo, G., & Sales, L. V. 2019, ApJ, 884, 54
Maraston, C. 2005, MNRAS, 362, 799
Marleau, F. R., Clancy, D., Habas, R., & Bianconi, M. 2017, A&A, 602, A28
Martins, L. P., Rodríguez-Ardila, A., de Souza, R., & Gruenwald, R. 2010, MNRAS, 406, 2168
Martins, L. P., Rodríguez-Ardila, A., Diniz, S., Riffel, R., & de Souza, R. 2013, MNRAS, 435, 2861
Mason, R. E., Rodríguez-Ardila, A., Martins, L., et al. 2015, ApJS, 217, 13
McLean, I. S., Becklin, E. E., Bendiksen, O., et al. 1998, Proc. SPIE, 3354, 566
Moran, E. C., Shahinyan, K., Sugarman, H. R., Vélez, D. O., & Eracleous, M. 2014, AJ, 148, 136
Morrissey, P., Matuszewski, M., Martin, D. C., et al. 2018, ApJ, 864, 93
Müller-Sánchez, F., Hicks, E. K. S., Malkan, M., et al. 2018, ApJ, 858, 48
Müller-Sánchez, F., Prieto, M. A., Hicks, E. K. S., et al. 2011, ApJ, 739, 69
Navarro, J. F., Frenk, C. S., & White, S. D. M. 1996, ApJ, 462, 563
Oke, J. B., Cohen, J. G., Carr, M., et al. 1995, PASP, 107, 375
Osterbrock, D. E., Tran, H. D., & Veilleux, S. 1992, ApJ, 389, 196
Peng, C. Y., Ho, L. C., Impey, C. D., & Rix, H.-W. 2002, AJ, 124, 266
Peng, C. Y., Ho, L. C., Impey, C. D., & Rix, H.-W. 2010, AJ, 139, 2097
Penny, S. J., Masters, K. L., Smethurst, R., et al. 2018, MNRAS, 476, 979
Penston, M. V., Fosbury, R. A. E., Boksenberg, A., Ward, M. J., & Wilson, A. S. 1984, MNRAS, 208, 347

Reines, A. E., Greene, J. E., & Geha, M. 2013, ApJ, 775, 116
Reines, A. E., & Volonteri, M. 2015, ApJ, 813, 82
Rich, J. A., Kewley, L. J., & Dopita, M. A. 2011, ApJ, 734, 87
Riffel, R., Pastoriza, M. G., Rodríguez-Ardila, A., & Bonatto, C. 2009, MNRAS, 400, 273
Riffel, R., Pastoriza, M. G., Rodríguez-Ardila, A., & Maraston, C. 2007, ApJL, 659, L103
Riffel, R., Rodríguez-Ardila, A., Aleman, I., et al. 2013, MNRAS, 430, 2002
Rockosi, C., Stover, R., Kibrick, R., et al. 2010, Proc. SPIE, 7735, 77350R
Rodríguez-Ardila, A., Prieto, M. A., Portilla, J. G., & Tejeiro, J. M. 2011, ApJ, 743, 100
Rodríguez-Ardila, A., Prieto, M. A., Viegas, S., & Gruenwald, R. 2006, ApJ, 653, 1098
Rodríguez-Ardila, A., Viegas, S. M., Pastoriza, M. G., & Prato, L. 2002, ApJ, 579, 214
Rupke, D. 2018, Galax, 6, 138
Rupke, D. S. N., Gültekin, K., & Veilleux, S. 2017, ApJ, 850, 40
Sanders, R. L., Shapley, A. E., Kriek, M., et al. 2016, ApJ, 816, 23
Sartori, L. F., Schawinski, K., Treister, E., et al. 2015, MNRAS, 454, 3722
Schinnerer, E., Eckart, A., & Tacconi, L. J. 1998, ApJ, 500, 147
Secrest, N. J., Satyapal, S., Gliozzi, M., et al. 2015, ApJ, 798, 38
Sexton, R. O., Matzko, W., Darden, N., Canalizo, G., & Gorjian, V. 2021, MNRAS, 500, 2871
Sharp, R. G., & Bland-Hawthorn, J. 2010, ApJ, 711, 818
Shirazi, M., & Brinchmann, J. 2012, MNRAS, 421, 1043
Simmonds, C., Bauer, F. E., Thuan, T. X., et al. 2016, A&A, 596, A64
U, V., Medling, A., Sanders, D., et al. 2013, ApJ, 775, 115
U, V., Medling, A. M., Inami, H., et al. 2019, ApJ, 871, 166
Veilleux, S. 1991a, ApJ, 369, 331
Veilleux, S. 1991b, ApJS, 75, 383
Veilleux, S., Cecil, G., & Bland-Hawthorn, J. 2005, ARA&A, 43, 769
Veilleux, S., Maiolino, R., Bolatto, A. D., & Aalto, S. 2020, A&A Rv, 28, 2
Veilleux, S., & Osterbrock, D. E. 1987, ApJS, 63, 295
Villar Martín, M., Bellocchi, E., Stern, J., et al. 2015, MNRAS, 454, 439
Wang, S., Liu, J., Qiu, Y., et al. 2016, ApJS, 224, 40
Wilson, J. C., Henderson, C. P., Herter, T. L., et al. 2004, Proc. SPIE, 5492, 1295